Relative importance of the mechanisms triggering the Eurasian ice sheet deglaciation in the GRISLI2.0 ice sheet model

Victor van Aalderen[1], Sylvie Charbit[1], Christophe Dumas[1], and Aurélien Quiquet[1]

[1]Laboratoire des Sciences du Climat et de l'Environnement, LSCE/IPSL, CEA-CNRS-UVSQ, Université Paris-Saclay, 91191 Gif-sur-Yvette cedex, France

Corresponding author: Victor van Aalderen (victor.van-aalderen@lsce.ipsl.fr)

Abstract

The last deglaciation (21000 to 8000 years BP) of the Eurasian ice sheet (EIS), is thought to have been responsible for a sea level rise of about 20 meters. While many studies have examined the timing and rate of the EIS retreat during this period, many questions remain about the key processes that triggered the EIS deglaciation 21,000 years ago. Due to its large marine-based parts in the Barents-Kara and British Isles sectors, BKIS is often considered as a potential analog of the current West Antarctic ice sheet (WAIS). Identifying the mechanisms that drove the EIS evolution might provide a better understanding of the processes at play in the West Antarctic destabilization. To investigate the relative impact of key drivers on the EIS destabilization we used the three-dimensional ice sheet model GRISLI (version 2.0) forced by climatic fields from five PMIP3/PMIP4 LGM simulations. In this study, we performed sensitivity experiments to test the response of the simulated Eurasian ice sheets to surface climate, oceanic temperatures (and thus basal melting under floating ice tongues) and sea level perturbations. Our results highlight that the EIS retreat simulated with the GRISLI model is primarily triggered by atmospheric warming. Increased atmospheric temperatures further amplify the sensitivity of the ice sheets to sub-shelf melting. These results contradict those of previous modelling studies mentioning the central role of basal melting on the deglaciation of the marine-based Barents-Kara ice sheet. However, we argue that the differences with previous works are mainly related to differences in the methodology followed to generate the initial LGM ice sheet. Due to the strong sensitivity of EIS to the atmospheric forcing highlighted with the GRISLI model and the limited extent of the confined ice shelves during the LGM, we conclude by questioning the analogy between EIS and the current WAIS. However, because of the expected rise in atmospheric temperatures, risk of hydrofracturing is increasing and could ultimately put the WAIS in a configuration similar to the past Eurasian ice sheet.

1 Introduction

During the last glacial maximum (LGM, 26-19 ka), the Eurasian ice complex was formed by the coalescence of three distinct ice sheets covering the British Isles, Fennoscandia and the Barents and Kara Seas. While the Fennoscandian ice sheet (FIS) was mostly grounded on the bedrock, the British Isles (BIIS) and Barents-Kara (BKIS) were mostly lying below sea level.

The Eurasian ice sheet (EIS) was influenced by various climate regimes with large differences between the western and eastern edges. Due to heat and moisture sources from the North Atlantic current, the British Isles and western Scandinavia were dominated by relatively warm and wet conditions contrasting with the more continental and drier climate in the eastern part of the EIS (Tierney et al., 2020). These various climatic influences prevailing over the three different ice sheets forming the Eurasian ice complex, may have resulted in different responses to variations in atmospheric and oceanic conditions. Over the last decade an active field of research has developed to identify the mechanisms behind the retreat of the Eurasian ice sheet during the last deglaciation, although no clear consensus has yet been reached. According to the recent study of Sejrup et al. (2022) the onset of the northern hemisphere deglaciation was primarily triggered by summer ablation resulting from increased summer insolation at 65 °N, and thus by changes in surface mass balance balance (SMB), defined as the difference between snow/ice accumulation and ablation.

On the other hand, studies based on modeling approaches suggest that the retreat of marine-based ice sheets could be driven by dynamical processes triggered by the melting of ice shelves (Pattyn et al., 2018). In fact, the relationship between oceanic temperatures and ice sheet mass balance has been confirmed and widely documented for the present-day WAIS. In particular, it has been shown that ocean warming plays a crucial role in accelerating Antarctic mass loss by enhancing basal melting and ice shelf thinning (Pritchard et al., 2012, Konrad et al., 2018, Pattyn et al., 2018; Rignot et al., 2019). This process may trigger a marine ice sheet instability when the bedrock is sloping towards the ice sheet interior. This instability translates into a sustained retreat of the grounding line and a significant glacier acceleration (Schoof, 2012). As large parts of BIIS and BKIS are marine based, their evolution could be driven by sub-shelf melting and potentially by the subsequent marine ice sheet instability. Based on the analysis of benthic and planktic foraminiferal assemblages, ice-rafted debris and radiocarbon dating, Rasmussen and Thomsen (2021) showed that the retreat of the ice in the Svalbard-Barents sector followed the deglacial oceanic, but also atmospheric, temperature changes. Relying on a first-order thermomechanical ice sheet model constrained by a variety of geomorphological, geophysical and geochronological data, Patton et al. (2017) found that the BIIS receded quite quickly in response to moderate increases in surface temperature. By contrast, the BKIS was rather affected by a combination of reduced precipitation and increased rates of iceberg calving. Other modeling studies have attempted to simulate the dynamics of the EIS during the last glacial period and the last deglaciation with the objective of better understanding the evolution of the ice sheet (Petrini et al., 2020; Alvarez-Solas et al., 2019). In a way similar to what is currently observed in West Antarctica, they suggest that large EIS variations are primarily due to the warming of the Atlantic Ocean leading to increased basal melting in the vicinity of the grounding line (Petrini et al., 2020; Alvarez-Solas et al., 2019). However, the models on which these studies are based have no specific treatment for computing ice velocities at the grounding line, making questionable their representation of the grounding line migration.

Because of the diversity of mechanisms that may have influenced the evolution of the three Eurasian ice sheets, the Eurasian ice complex is an interesting case study to investigate the different mechanisms responsible for the ice sheet retreat. As both BKIS and BIIS are marine-based (Svendsen et al., 2004, Gandy et al., 2018, 2021), they are likely to be more sensitive to oceanic temperature variations. Special attention can be given to BKIS because it has often been considered as a potential analogue of the present-day WAIS (Gudlaugsson et al., 2017, Andreassen and Winsborrow, 2009, Mercer, 1970) due to common features such as the ice volume and a bedrock largely grounded below sea level with an upstream deepening (Amante et al., 2009). As a result, in-depth investigations of the BKIS behavior at the LGM can help to better understand the present-day changes and future evolution of West Antarctica.

This wide range of hypotheses regarding the different processes responsible for the EIS destabilization (i.e atmospheric climate, oceanic climate or both) confirms that there is still a lot of unknowns in the EIS dynamics during the last deglaciation and that the debate is not closed. Progress has been made in ice sheet modeling with the development of new generation models computing the full Stocks flow equations. For example, with a refined model resolution near the grounding line, Gandy et al., (2018, 2021) have quantified the impact of oceanic temperatures on the grounding line dynamics and investigated the potential occurrence and effect of the marine ice sheet instability. However, as the computation time is considerably increased, they focus only on specific sectors (i.e. North Sea) and thus do not consider the impact of the other interconnected ice sheets.

In this paper, we present simulations of the entire Eurasian ice complex during the LGM using the three-dimensional GRISLI2.0 (GRenoble Ice Shelf and Land Ice) ice sheet model (Quiquet et al., 2018). GRISLI2.0 includes an explicit calculation of the ice flux at the grounding line derived from the analytical formulation provided by Tsai et al. (2015), which is expected to account for the representation of the marine ice sheet instability. Our ultimate objective is not to reproduce the exact timing of the last deglaciation of the EIS but rather to explore the sensitivity of EIS to various perturbations using the GRISLI ice model.

Starting from its LGM geometry, we investigate the EIS sensitivity to perturbations of surface air temperature, precipitation rate, basal melting, and sea level to better understand their relative contribution to the EIS destabilization. In this work, the GRISLI2.0 ice sheet model was forced by a panel of ten different climates from the Paleoclimate Modelling Intercomparison Project (PMIP) database (Abe-Ouchi et al., 2015; Kageyama et al., 2021).

The paper is organized as follows. Section 2 provides a description of the basic equations of the GRISLI2.0 ice sheet model. It also includes a presentation of the climate forcing and the experimental setup of the LGM and sensitivity experiments. Section 3 compares our different reconstructions of the EIS at the LGM. The results of the sensitivity experiments are presented in section 4 and discussed in section 5. Concluding remarks are given in section 6.

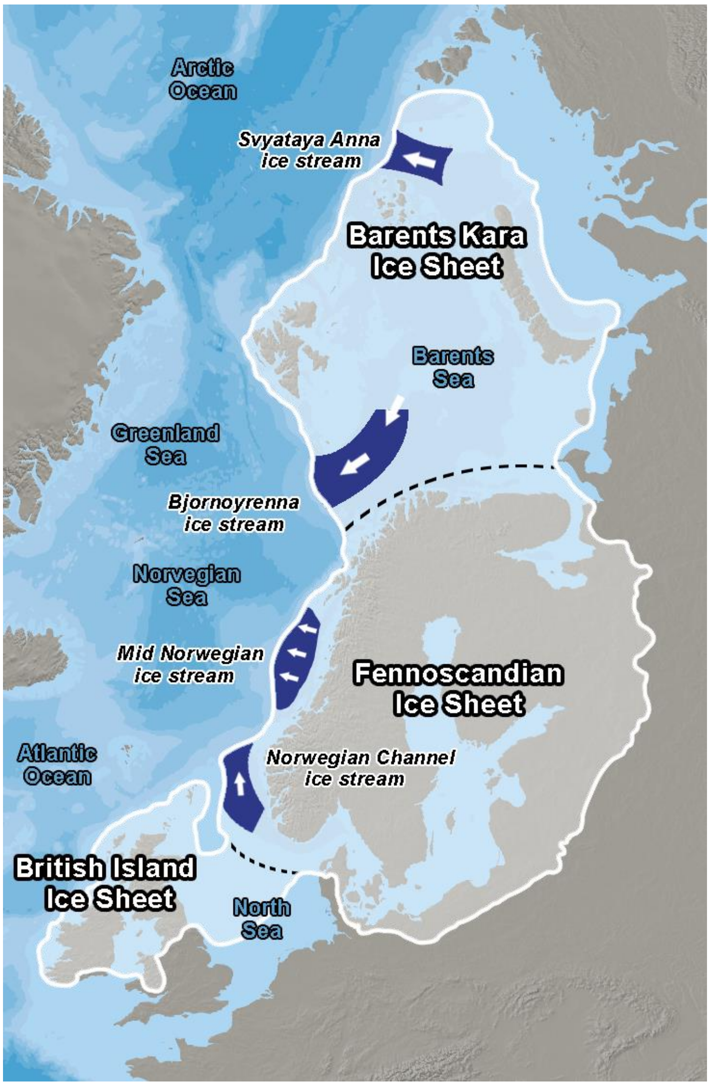

Figure 1: Map of the Eurasian Ice Sheet at the LGM. The white line is the most credible ice extent of the Eurasian ice sheet at the LGM according to the DATED-1 compilation (Hughes et al., 2016). Dark blue shaded areas correspond to the location of the main ice streams (Dowdeswell et al., 2016; Stokes and Clark, 2001), and dotted black lines are delimitations between the Fennoscandian, the Barents-Kara, and the British Isles ice sheets.

2. Model description and experimental set-up

2.1 The GRISLI ice sheet model

In this study, we use the 3D thermomechanical ice sheet model GRISLI2.0 (referred hereafter to as GRISLI) run on a Cartesian grid with a horizontal resolution of 20 km x 20 km, corresponding to 177 x 257 grid points.

This ice sheet model was initially built to study the Antarctic ice sheet behavior during glacial-interglacial cycles (Ritz et al. 2001). It was then adapted to the Northern Hemisphere ice sheets (e.g. Peyaud et al., 2007) and tested under various climatic conditions (Ladant et al., 2014, Le clec'h et al. 2019, Colleoni et al., 2014, Beghin et al. 2014). GRISLI also took part in the Ice Sheet Model Intercomparison Project (ISMIP6) (Goelzer et al.; 2020, Seroussi et al., 2020, Quiquet and Dumas, 2021a, 2021b) to investigate future sea level changes (Nowicki et al. 2020). A full description of GRISLI can be found in Quiquet et al. (2018). Here, we only remind the basic principles of the model. The main modification in this new version of GRISLI compared to previous ones (Ritz et al., 2001; Peyaud et al., 2007) is the implementation of analytical formulations of the flux at the grounding line leading to a better representation of the grounding line migration.

The evolution of the ice sheet geometry depends on the ice sheet surface mass balance, ice dynamics and isostatic adjustment. Assuming that ice is an incompressible material, changes in ice thickness with time are given by the mass balance equation:

$$\frac{dH}{dt} = SMB - Bmelt - \nabla(UH) \qquad (1)$$

with H being the local ice thickness, SMB the surface mass balance, $Bmelt$ the basal melting in grounded ice areas and under the ice shelves, U the vertical average velocity, and ∇ (UH) the ice flux divergence.

The ice velocity is calculated from the sum of the shallow ice approximation (SIA) and the shallow shelf approximation (SSA) components (Winkelmann et al., 2011). Both approximations take advantage of the small aspect ratio of the ice sheets (Hutter, 1983). The SIA assumes that the longitudinal shear stresses can be neglected compared to the vertical shear stresses and holds for all ice sheet regions where the gravity-driven flow induces a slow motion of the ice (Hutter, 1983). Conversely, the SSA neglects the vertical shear stresses compared to the longitudinal shear stresses, which is generally valid for floating ice shelves (MacAyeal, 1989) and to some extent for fast-flowing ice streams. As a result, the total ice sheet domain can be separated into three regions: floating ice shelves where the ice velocity is computed with the SSA, cold-base areas governed by the SIA, and finally, the temperate-base grounded ice, where the ice velocity is computed as the sum of the SIA and SSA components.

The basal friction for the temperate base areas is assumed to follow a linear friction law:

$$\tau_b = -\beta U_b \qquad (2)$$

where τ_b is the basal shear stress, U_b the basal velocity and β the basal drag coefficient. The basal drag coefficient depends on the effective water pressure (N), i.e. the difference between water pressure and ice pressure, and on an internal constant parameter (C_f= 1.5 10^{-6} m yr^{-1}):

$$\beta = C_f N \qquad (3)$$

The effective pressure N depends on the groundwater hydrology which is calculated according to Darcy's law (Quiquet et al., 2018).

At the base of the grounded ice sheet, the basal temperature is also critically dependent on the geothermal heat flux which is given here by the distribution of Shapiro and Ritzwoller (2004).

To simulate artificially the effect of ice anisotropy on the ice velocity, most ice sheet models use an enhancement factor in the non-linear viscous flow law that relates deformation rates and stresses with values generally ranging between 1 and 5. In GRISLI, two enhancement factors are considered (E_{SIA} and E_{SSA}). E_{SIA} is applied to the SIA component of the velocity to increase (E_{SIA}>1) the deformation induced by vertical shearing. Conversely E_{SSA} is applied to the SSA component of the velocity to reduce (E_{SSA}<1) the deformation due to longitudinal stresses. The model parameters used in this study are the same as those used in Quiquet et al. (2021c) with the exception of E_{SIA} and C_f fixed respectively to 5 (instead of 1.8) and 1.5 10^{-6} m yr^{-1} (instead of 1.5 10^{-3} m yr^{-1}). Those parameters have been chosen for a better match between the simulated EIS ice volume at the LGM and the geologically-constrained reconstructions (see Section 2.3).

The horizontal resolution used in this study is too coarse to simulate explicitly the grounding line migration (Durand et al., 2009). To circumvent this drawback, we use the analytical formulation from Tsai et al. (2015), in which the ice flux at the grounding line is computed as a function of the ice thickness and a backforce coefficient accounting for the buttressing effect of the ice shelves. In this way, a flow at the grounding line can be simulated with a lower resolution allowing time saving in the simulations. Technical details on this implementation in the GRISLI model are given in Quiquet et al. (2018).

At the ice shelf front, calving is computed using a simple ice thickness criterion by prescribing a minimal ice thickness set to 250 m below which ice is calved.

In the GRISLI model, the isostatic response to ice load is handled by an Elastic-Lithosphere-Relaxed-Asthenosphere (ELRA) model (Le Meur and Huybrechts, 1996). The relaxation time of the lithosphere is set to 3000 years.

2.2 Climate forcing

We forced GRISLI with the absolute climatic fields from general circulation model (GCM) outputs of the PMIP3/PMIP4 database (Kageyama et al., 2021). All the GCMs for which LGM simulations were available at the time of writing the manuscript have been selected (see Table 1).

Table 1: PMIP3 and PMIP4 models used to force GRISLI. The fourth column indicates the choice of the ice sheet boundary condition at the LGM for each GCM simulation. ice sheet reconstructions used as a boundary condition of the GCM simulations at the LGM.

model	References	PMIP/CMIP	Boundary condition
MPI-ESM-P	Adloff et al. (2018)	CMIP5 PMIP3	PMIP3 ice sheet
MRI-CGM3	Yukimoto S et al. (2012)	CMIP5 PMIP3	PMIP3 ice sheet
MIROC-ESM	Sueyoshi et al. (2013)	CMIP5 PMIP3	PMIP3 ice sheet
CNRM-CM5	Voldoire et al. (2013)	CMIP5 PMIP3	PMIP3 ice sheet
GISS-E2-R	Ullman et al. (2014)	CMIP5 PMIP3	PMIP3 ice sheet
FGOALS-g2	Zheng and Yu (2014)	CMIP5 PMIP3	PMIP3 ice sheet
IPSL-CM5A-LR	Dufresne et al. (2013)	CMIP5 PMIP3	PMIP3 ice sheet
IPSL-CM5A2	Sepulchre et al. (2020)	CMIP6 PMIP4	ICE-6G_C
MIROC-ES2L	Hajima et al. (2020)	CMIP6 PMIP4	ICE-6G_C
MPI-ESM1.2	Mauritsen et al. (2019)	CMIP6 PMIP4	ICE-6G_C

Monthly surface air temperatures and solid monthly precipitation are used to compute the surface mass balance defined as the difference between snow/ice accumulation and ablation. Ablation is calculated using a positive degree-day (PDD) method following the formulation of Tarasov and Peltier (2002), where the degree-day factors,

C_{ice} and C_{snow}, depend on the mean July surface air temperature**.** Snow accumulation is calculated from the total precipitation (rain and snow), considering only months where monthly temperatures are under the melting point.

Due to the differences between GCM and GRISLI resolutions, the GCM outputs are bi-linearly interpolated onto the ice sheet model grid. In addition, to account for orography differences between GRISLI and the GCMs, the surface air temperatures of the GCMs are corrected using a constant vertical temperature gradient λ = 7 °C km^{-1}:

$$T(t)_{GRISLI} = T_{GCM}^{LGM} - \lambda(S(t) - S_{GCM}^{LGM}) \qquad (4)$$

where $T(t)_{GRISLI}$ is the time-dependent surface air temperature at the surface elevation $S(t)$ simulated by the ice sheet model, and T_{GCM}^{LGM} and S_{GCM}^{LGM} are the LGM surface air temperature and orography computed by the GCMs. This temperature correction induces a change in precipitation which is computed following the Clausius-Clapeyron formulation for an ideal gas:

$$pr(t)_{GRISLI} = pr_{GCM}^{LGM} * \exp\left(\omega * (T(t)_{GRISLI} - T_{GCM}^{LGM}) \right) \quad (5)$$

where $pr(t)_{GRISLI}$ is the precipitation calculated by GRISLI at each time step and pr_{GCM}^{LGM} is the LGM precipitation computed by the GCM and interpolated on the GRISLI grid. ω is the precipitation ratio to temperature change and is fixed to 0.11 °C^{-1} (Quiquet et al., 2013).

Following DeConto and Pollard (2012), the sub-shelf melt rate (OM) is computed using ocean temperature and salinity:

$$OM = K_t \frac{\rho_w C_w}{\rho_i L_f} \left| T_o - T_f \right| \left(T_o - T_f \right) \quad (6)$$

where K_t is called the transfer factor and is set to 7 m yr^{-1} °C^{-1} in the baseline experiments as in DeConto and Pollard (2012), ρ_w the ocean water density, ρ_i ice density, L_f the latent heat of ice fusion, C_w the specific heat of ocean water and T_o is the local ocean temperature. T_f is the local freezing point temperature, depending on the ocean salinity (S) and computed by the Beckmann and Goosse (2003) parameterization:

$$T_f = 0.0939°C - S \times 0.057°C + z \times 7.6410^{-4}°C \qquad (7)$$

where z is the ocean depth.

A difficulty related to the oceanic forcing fields is that the GCMs do not provide any oceanic information outside their land-sea mask and under the ice shelves. To fill these gaps, we performed a classical near neighbour horizontal extrapolation of temperature and salinity except that we perform this extrapolation within 10 sectors independently. These sectors roughly correspond to drainage basins (Fig. S1). The definition of these basins is based on bedrock topographic features and LGM ice elevation and is somehow comparable to the approach followed by Zwally et al. (2015) for Antarctica. The horizontal extrapolation is performed for each individual vertical layer, without any vertical interpolation. This extrapolation method provides information on temperature and salinity within the entire ice shelf cavity for each vertical level of the GCMs. These temperature and salinity fields are then used to compute the sub-shelf melt rate (Eq. 6), using a linear vertical interpolation between the two oceanic layers bounding the ice shelf depth. The only exception is when the PMIP3/PMIP4 simulations do not provide data in a given sector. In this case, a constant and homogeneous basal melting value of 0.1 m yr^{-1} is prescribed. This mainly occurs in the continental southern flanks of the Eurasian ice sheet.

In GRISLI, each grid point can either be a floating or a grounded ice point. To account for the fact that the sub-shelf melt rate is higher in the vicinity of the grounded line (Beckmann and Goose, 2003) and due to the coarse resolution of the model, we apply a fraction of the neighboring floating sub-shelf melt rate to the last grounded point as in De Conto and Pollard (2012). This approach allows to take the potential influence of the ocean into account.

The main parameters and parameterizations used in this study are shown in Table 2 and Table 3.

Table 2: Model parameters of the GRISLI ice-sheet model used in this study

Parameters	Identifier name	Value
Enhancement factor (SIA)	E_{SIA}	5
Enhancement factor (SSA)	E_{SSA}	1
Atmospheric temperature lapse rate	λ	7 °C km^{-1}
Precipitation ratio to temperature change	ω	0.11 °C^{-1}
Oceanic heat transfer factor	K_t	7 m yr^{-1} °C^{-1}
Thickness threshold for the calving criterion	H_{cut}	250 m
Relaxation time of the asthenosphere	R_{time}	3000 years
Basal drag parameter	C_f	1.5 10^{-6} m yr^{-1}

Table 3: Parameterizations of the GRISLI ice-sheet model used in this study

Parameterizations	References
Positive degree-days	Tarasov and Peltier (2002)
Basal melting below ice shelves	Deconto and Pollard (2012)
Flux at the grounding line	Tsai et al. (2015)
Basal friction law	Linear law / Weertman (1957)

2.3 LGM equilibrium

As mentioned above, the main objective of the present paper is to investigate the mechanisms responsible for the EIS retreat from its LGM configuration. To do this, a preliminary step is to build the EIS at the LGM.

We performed ten 100 000-year spin-up experiments (one for each GCM) forced by a constant LGM climate provided by the ten GCMs. Simulations start with no ice sheet and the eustatic sea level is prescribed at 120 m below the present level. The initial bedrock topography corresponds to the present-day topography from ETOPO1 (Amante et al., 2009). This procedure is required to obtain internal ice sheet conditions in equilibrium with the climate forcing and to examine whether the LGM climate can build and maintain the EIS when it is used as input to the GRISLI ice sheet model. From this climate forcing ensemble, we only selected those leading to LGM ice sheets in a reasonable agreement with the most credible ice extent in the DATED-1 database (Hughes et al., 2016) and with the geologically-constrained ice thickness reconstructions, namely ICE-6G_C (Peltier et al., 2015), GLAC-1D (Briggs et al., 2014; Tarasov et al., 2012; Tarasov and Peltier, 2002), and ANU (Lambeck et al., 1995, 1996, 2010).

2.4 Sensitivity experiments

To quantify the relative importance of the three main drivers (i.e., surface mass balance, sub-shelf melt rate, and sea level) of the EIS retreat, we applied time-constant perturbations on the atmospheric and oceanic GCM forcings, and we changed the prescribed sea level. The perturbed simulations are run for 10000 years. We analysed the response at year 1000 of the simulation to investigate the impacts of climate changes that may have occurred at the beginning of the deglaciation and at year 10,000 to examine the sensitivity of EIS on longer time scales.

In the first series of experiments (EXP1), we investigate the effect of SMB changes by increasing surface air temperatures. During the last deglaciation (21 – 8 ka), the mean annual global surface air temperature increased by 4,5° ± 0.9° (Annan et al., 2022). In order to simulate a range of anomalies representative of the onset of the last deglaciation, we chose to apply perturbations from 1 to 5 °C to the mean annual GCM forcing fields, without accounting for related changes in precipitation (see Eq 5).

We know from the Clausius-Clapeyron relationship that the water content in the atmosphere is directly related to atmospheric temperature. An increase in atmospheric temperature can therefore lead to an increase in precipitation. This is what is currently being observed in the eastern Antarctica (Frieler et al., 2015). As a result, the increase in precipitation in response to increased temperatures (Eq. 5) is considered in the second set of experiments (EXP2).

The third series of experiments (EXP3) is designed to assess the role of oceanic forcing on the EIS stability. Because the basal melting below the ice shelves depends linearly on the Kt transfer coefficient and is a quadratic function of the oceanic temperatures, we performed two sub-series of experiments by modifying either the Kt values (EXP3.1) without modifying the oceanic temperatures, or by applying perturbations to the oceanic temperatures (EXP3.2). Observations below the Antarctic ice shelves show that the basal melting rate ranges from 0 to 35 m yr^{-1} for oceanic temperatures between -2 °C and 2 °C (Holland et al., 2008). This wide range of basal melting rate values reflects the complexity of such a process that can only be partially represented with simple parameterizations (Eq. 6). The Kt coefficient is thus largely uncertain. Therefore, to investigate changes in the EIS sensitivity to the amplitude of basal melting, we first use a wide range of values for this transfer coefficient, i.e. between 10 and 50 m yr^{-1}°C^{-1}.

The mean global sea surface temperature anomaly inferred from the MARGO project (MARGO project members, 2009) between the Late Holocene and the LGM is 1.9 ±1.8°C consistent with the findings (~2.7°C) of Tierney et al. (2020). In the early phase of the deglaciation, the ocean warming was probably less than that of the Late Holocene. Therefore, for the EXP3.2 experiments, we first apply perturbations of 0.5°C, 1.0°C, 1.5°C to the oceanic temperatures (same perturbation on all vertical levels) and we fix the Kt coefficient to 7 m °C^{-1} yr^{-1}. In the transient simulation of the last deglaciation performed by Liu et al. (2009), large increases in oceanic temperatures are obtained. For example, a +9°C warming is obtained in the BJR sector at 500-600 m ocean depth and almost 7.5°C in the SA sector at 400-500 m. To reproduce the large increase in the subsurface ocean temperature obtained in Liu et al. (2009), we performed additional sensitivity experiments with perturbations of 7.5°C and 10°C applied in the entire oceanic column.

Atmospheric and oceanic temperatures are the two main factors potentially responsible for the destabilization of marine ice sheets. Thus, the fourth series of experiments (EXP4) combines surface air temperature perturbations (ΔT = +2°C, +3°C, and +4°C) with basal melting rate perturbations (Kt = 10, 15 and 25 m yr^{-1} $°C^{-1}$).

In the fifth set of experiments (EXP5), we also explore the EIS sensitivity to sea level. Indeed, sea level rise favors the retreat of the grounding line and is therefore another potential driver of the MISI. At the beginning of the deglaciation, the global sea level increased by more than 10 m (Carlson and Clark, 2012) raising the global sea level from -120 m to -110 m compared to the present-day eustatic sea level. This abrupt change may have played an important role in the destabilisation of the ice sheet. On the other hand, Gowan et al., (2021) shows that the local sea level around the EIS margin displays a significant spread at the LGM, from -70 m to -140 m, compared to the present-day level and can abruptly change in response to variations in the land-ice mass distribution. Consequently, to better explore the EIS sensitivity to both global mean sea level and local sea level at the beginning of the last deglaciation, we apply moderate (-115 m, -110 m, and -105 m) and large (-90 m, -60 m, -30 m, and 0 m) sea level perturbations with respect to the present day.

3. Available ice sheet reconstructions and ice streams signature

3.1 Ice sheet geometry

The DATED-1 database is based on evidence found in the existing literature and retrieved from various geological materials (e.g., terrestrial plant macrofossils, foraminifera, speleothems, bones…) analysed with a range of dating methods. Based on these data, the DATED-1 compilation provides three different scenarios for the maximal, minimal and most credible EIS extent. The GLAC-1D, ICE-6G_C, and ANU reconstructions are based on inverse modeling approaches constrained by GPS data, relative sea level and geomorphological data.

The main differences in the three DATED-1 scenarios at the LGM (Hughes et al., 2016) are related to the potential BIIS-FIS connection (or disconnection), the southern continental limit of the FIS and the eastern limit of BKIS (Fig. 2a). Only the minimum scenario suggests the absence of ice between the BIIS and FIS.

The GLAC-1D reconstruction agrees well with the most credible DATED-1 scenario, despite a slightly greater ice extent in most of the Fennoscandian regions and a smaller extent in the Taymyr Peninsula (in the easternmost part of the BKIS, Fig. 2d). This contrasts with the ANU and ICE-6G_C reconstructions whose ice limit goes beyond that of the most credible DATED-1 scenario.

The differences between the three geologically-constrained reconstructions are due to differences in the inverse methods used to estimate the ice thickness, to the geological and geomorphological data considered to infer the ice extent, and to different choices regarding the Earth rheology. This translates into differences in the altitude of the EIS. For example, in the ANU and GLAC-1D reconstructions, the FIS peaks at 3000-3500 m, while BKIS does not exceed 2500 m (2000 m for GLAC-1D). By contrast, ICE-6G_C provides a larger ice thickness over the BKIS sector (2500-3000 m) than over Fennoscandia.

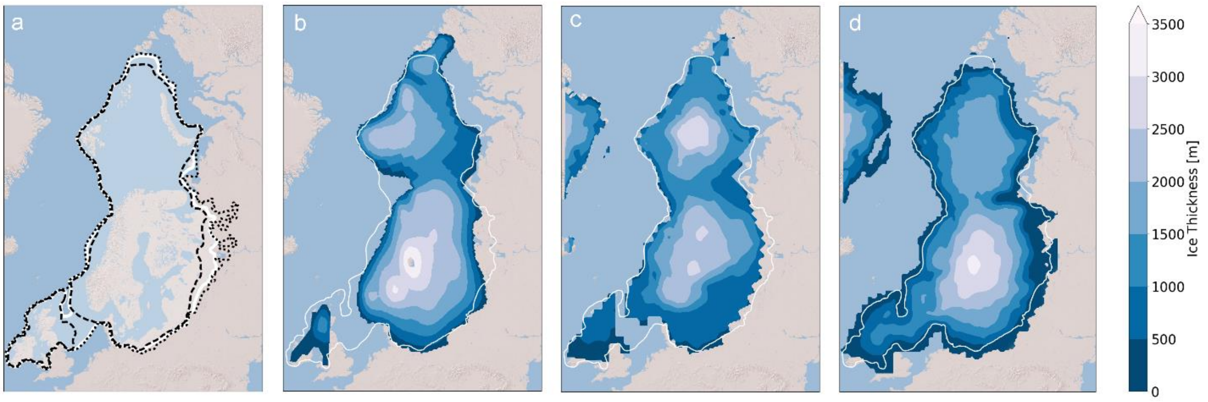

Figure 2: a/ Ice sheet extent at the LGM derived from the DATED-1 compilation (Hughes et al., 2016). The maximum and the minimum scenarios of the ice extent are represented by the dotted and the dashed lines respectively. b/ Ice thickness at the LGM provided by the ANU reconstruction (Lambeck et al., 1995, 1996, 2010; Abe-Ouchi et al., 2015). c/ Same as b/ for the ICE-6G_C reconstruction (Peltier et al., 2015). d/ Same as b/ for the GLAC-1D reconstruction (Briggs et al., 2014; Tarasov et al., 2012; Tarasov and Peltier, 2002). In the four panels, the white line corresponds to the most credible scenario of the ice extent at the LGM derived from the DATED-1 compilation (Hughes et al., 2016).

3.2 Ice stream signature

Ice streams also play a key role in ice sheet dynamics and in featuring ice sheet geometry (Pritchard et al., 2009). It is therefore crucial that the dynamics of the simulated ice sheets is consistent with reconstructions. The signature of ice streams can be inferred from geomorphological observations in the Barents Sea, in particular those of the Bjornoyrenna (BJR) and Svyataya Anna (SA) ice streams (Fig. 1) (Polyak et al., 1997; Andreassen and Winsborrow, 2009; Dowdeswell et al., 2016,2021; Szuman et al., 2021). Other geomorphological observations strongly suggest the existence of paleo ice streams in the FIS, such as the Mid-Norwegian (MN) ice stream (Stokes and Clark, 2001), and the Norwegian Channel (NC) ice stream between the FIS and BIIS (Sejrup et al., 1994; Svendsen et al., 2015; Stokes and Clark, 2001).

4. Results

4.1 LGM equilibrium

At the end of the 100 000-year spin-up simulations, a wide range of ice sheet geometries is obtained (Fig. 3). In the same way as Niu et al. (2019), we show that simulations performed with CNRM-CM5 and MRI-CGM3 do not succeed in maintaining ice cover over Eurasia as extended as in the reconstructions. In addition, we show that the simulation forced by MIROC-ES2L also fails to form an ice sheet.

This is primarily explained by high positive summer surface air temperatures simulated by the three models in most parts of the EIS compared to the other models, with temperature anomalies ranging between +4.7°C and +11.7°C (Fig. 4). Conversely, with the GISS-E2-R and FGOALS-g2 models, significant ice thickness is built east and south of BKIS because of strong negative mean summer temperatures in this area (Fig. 4).

Therefore, we discarded these models and only selected those (MPI-ESM-P, MIROC-ESM, IPSL-CM5A2, IPSL-CM5-LR, and MPI-ESM1.2) providing ice sheet geometries in a relatively good agreement with the reconstructions.

The five selected ice sheets do not show significant differences (Fig 3). The FIS peaks at 2500-3000 m, while the BKIS is lower (2000 – 2500 m) due to a drier atmosphere compared to that overlying the Fennoscandian region (Fig. 5). The simulated FIS agrees with the ICE-6G_C reconstruction despite a flatter dome simulated with MPI-ESM-P, about 500 m lower compared to GLAC-1D and ANU. Conversely, the BKIS maximum altitude simulated by GRISLI is underestimated compared to ICE-6G_C while it is in good agreement with the two other reconstructions. The BKIS margins bordering the Greenland and Norwegian Seas and the Arctic Ocean generally match with the most credible DATED-1 scenario of the ice extent. However, in the five GRISLI simulations, the ice extent is too large in the eastern and southern edges compared to DATED-1.

The most likely cause of this mismatch is related to the imprint of the ice sheet reconstructions used as boundary conditions of GCM simulations. Indeed, both the ice sheet reconstruction used for PMIP3 simulations (not shown) and ICE-6G_C (Fig. 2c) used in PMIP4 runs overestimate the ice extent in the region of the Taimyr Peninsula. This results in an enhanced cooling favoring the simulated ice expansion in this area. This effect can be amplified by the projections of the ice sheet reconstructions on the coarser GCM grid that may produce an artificial spread of the ice sheet mask, causing further a too extended cooling. Another source of disagreement between DATED-1 and the simulated ice sheets can be due to the representation the jet stream and planetary waves in the coarse resolution climate models, such as the PMIP models. Indeed, such large-scale atmospheric features directly impact the simulated precipitation and temperatures and may cause too much precipitation or too much cooling if improperly represented (Löfverström and Liakka, 2018).

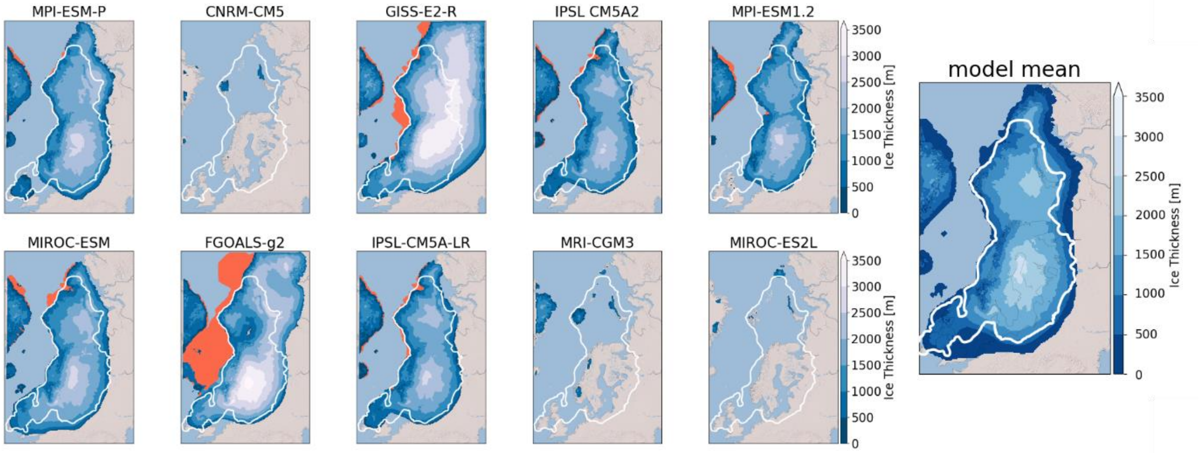

Figure 3: Ice thickness at the end of the 100 000-year simulation for the different GCMs used as forcing of the GRISLI ice sheet model. The white line is the most credible extent derived from the DATED-1 compilation and the orange shaded areas are the simulated ice shelves. The multi model mean of the five selected ice sheet is shown in the right panel.

For the five selected GCMs, areas with high ice velocities are simulated in the BKIS region (Fig. 6). The highest velocities are obtained for the SA, BJR, NC and MN ice streams and can exceed 1000 m yr^{-1}. In addition, the BJR ice stream shows a large extension from the center of BKIS, with velocities between 75 to 200 m yr^{-1}, to the edge of BKIS. The location of the main fast flowing areas is consistent with empirical evidence based on observations of submarine landforms (Dowdeswell et al., 2016; Stokes and Clark, 2001). It is also interesting to mention that ice velocities of similar magnitude in the present-day Antarctic and Greenland ice sheets have been revealed thanks to radar observations (Solgaard et al., 2021; Mouginot et al., 2019).

Overall, our five remaining simulated ice sheets show a reasonable agreement with the different reconstructions constrained by geological and geomorphological observations, both in terms of ice extent and ice thickness as well as dynamical characteristics. The observed differences with the reconstructions remain within the range of uncertainties, which is itself illustrated by the differences between the three reconstructions GLAC-1D, ANU and ICE-6G_C and by the three ice extent scenarios from the DATED-1 compilation.

This allows us to use the five spin-up GRISLI experiments (forced by MPI-ESM-P, MIROC-ESM, IPSL-CM5A2, IPSL-CM5-LR, and MPI-ESM1.2) as a starting point to test the sensitivity of the EIS to atmospheric, oceanic and sea level forcings.

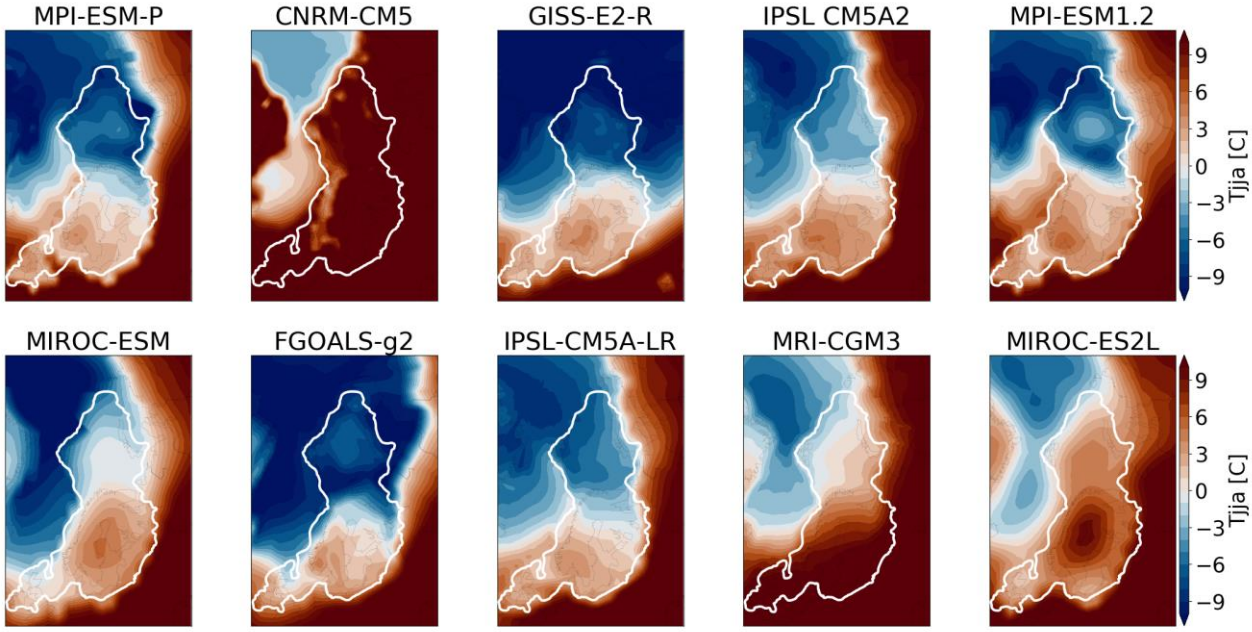

Figure 4: Mean summer (JJA) surface air temperature at 21 ka simulated by each GCM at the sea level and interpolated on the GRISLI grid. The white line represents the ice extent as defined by the most credible DATED-1 scenario.

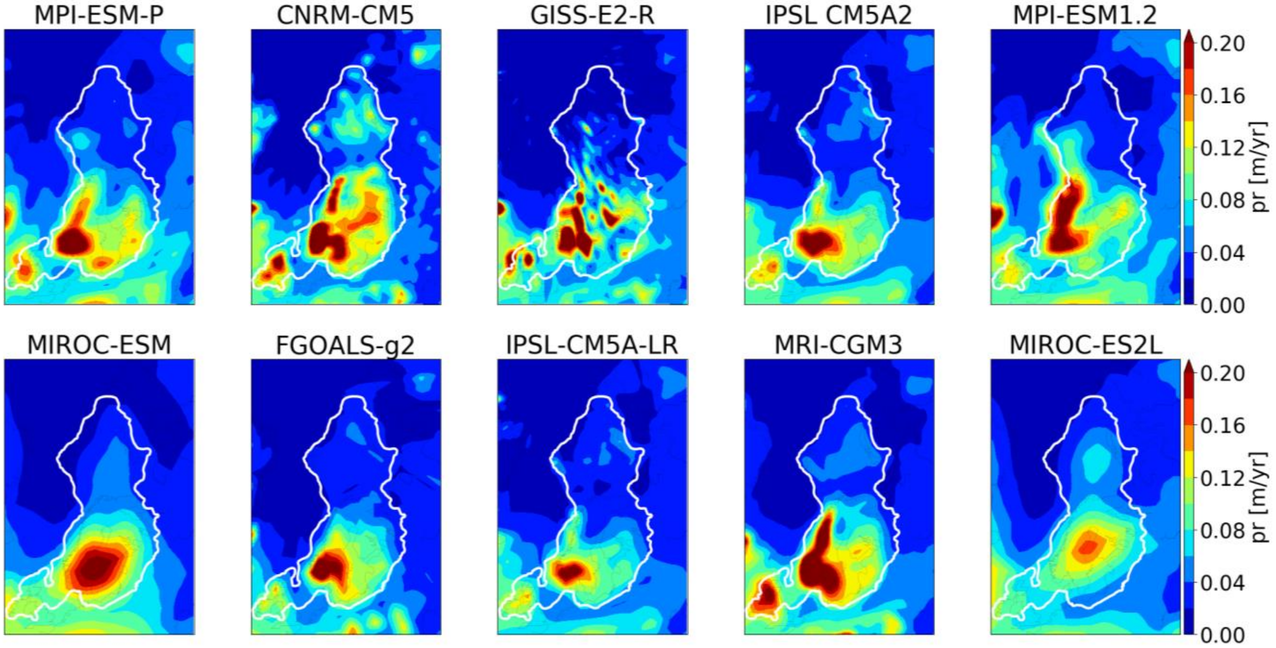

Figure 5: Same as Figure 4 for the mean annual precipitation.

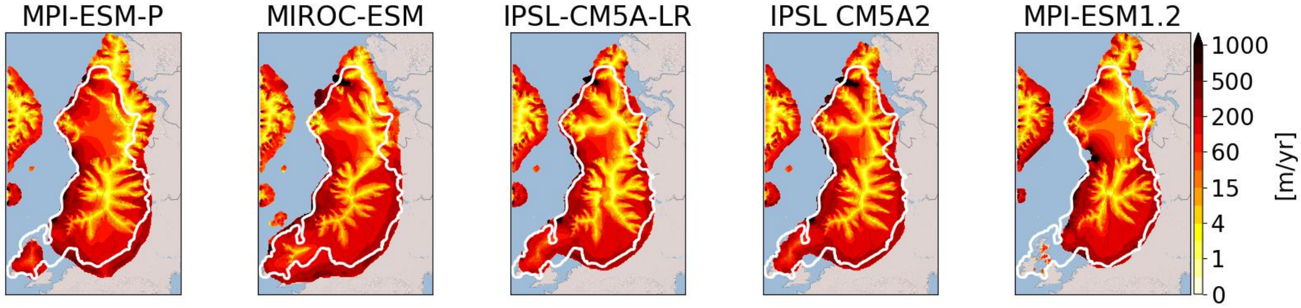

Figure 6: Simulated ice velocities at the end of the 100 000-year LGM simulation. The solid white line represents the most credible ice extent from the DATED-1 compilation.

4.2. Sensitivity experiments

In the following, we investigate the sensitivity of the Eurasian ice sheet to the potential drivers of ice sheet retreat: atmospheric changes responsible for SMB changes (i.e., temperature and snow accumulation to the first order), oceanic changes (sub-shelf melt rate) and sea level changes.

4.2.1 EXP1: Surface air temperature

The aim of this section is to investigate the sensitivity of EIS to a temperature rise. For each temperature perturbation (T_{add} = 1 to 5°C) applied uniformly on the monthly mean surface air temperatures, Figure 7 displays for the multi-model mean the percentage of the ice thickness lost after 1000 years with respect to the initial configuration. The results are plotted for the largest ice sheet mask. This mask corresponds to all areas where ice has been simulated in at least one of the 5 simulations. This means that multi-model means are computed with 1, 2, 3, 4 or 5 models involved, depending on the ice sheet mask of each individual model.

For T_{add} = 1 °C, the response of the Eurasian ice sheets is weak, except for the British Isles sector (Fig 7) for which mean JJA temperatures of the five selected GCMs are close to the melting point (Fig. 4). Substantial ice losses are also simulated in the FIS margins for temperature rise greater than 1 °C leading to a progressive retreat of the edge of the ice sheet as the temperature increases. The sensitivity of the BIIS and FIS regions to these temperature perturbations is explained by a shift from positive to negative SMB values when temperature increases (Fig. SP2). By contrast, as the BKIS is located in colder areas, larger temperature perturbations (3 to 5 °C) are necessary to initiate the ice sheet's retreat. The southern BKIS margin appears the most sensitive region, followed by the region of the SA ice stream. In the SA sector, ice thickness losses between 30 % (Tadd = +3°C) to 50 % (Tadd = +5°C) are obtained. In the BJR sector, ice losses are only simulated for large temperature perturbations.

However, it is worth mentioning that for a given temperature perturbation, significant differences in the behavior of the five simulated ice sheets can be observed. To illustrate these differences, we plotted for each simulation, the percentage of the ice thickness lost after 1000 years with respect to the initial configuration (Fig SP3). The most sensitive regions to surface air temperature, namely the FIS margins and the SA/BJR sectors, are the locations where inter-model differences in ice thickness losses are the most significant and are amplified with temperature increase. In the BJR sector, the retreat of the ice sheet is simulated for perturbations of 4°C with three GCM forcings (MIROC-ESM, IPSL-CM5A-LR and IPSL-CM5A2, Fig SP3), while this sector is stable with the two other forcings (MPI-ESM-P and MPI-ESM1.2) under this temperature perturbation. In the SA sector, the MIROC-ESM-P forcing produces a retreat from a temperature anomaly of 2°C, but for the IPSL-CM5A-LR and IPSL-CM5A2 forcings the retreat is only triggered for T_{add} = 3 °C. By contrast, the two versions of the MPI-ESM produce a more stable ice sheet in the SA sector since, even with a 5 °C temperature perturbation, the ice retreat is not triggered within the 1000 years of simulation.

The lower sensitivity of BJR sector, compared to the SA sector, can be explained (at least partly) by the topography differences between these two regions. Actually, the initial topography of each GCM (not shown) exhibits a trough in the SA sector which does not appear in the region of the BJR ice stream. The lower surface topography in the SA sector is accompanied by higher surface temperatures and thus to larger ice losses when temperature perturbations are applied (Fig. SP3). Moreover, the difference in the sensitivity of the BJR and SA sectors can be also explained by the higher precipitation rate in the BJR sector (between 0.2 to 0.5 m yr^{-1} for the BJR ice stream and less than 0.2 m yr^{-1} for the SA sector, Fig. 5), which can partly counteract the effect of temperature increase on ice mass loss.

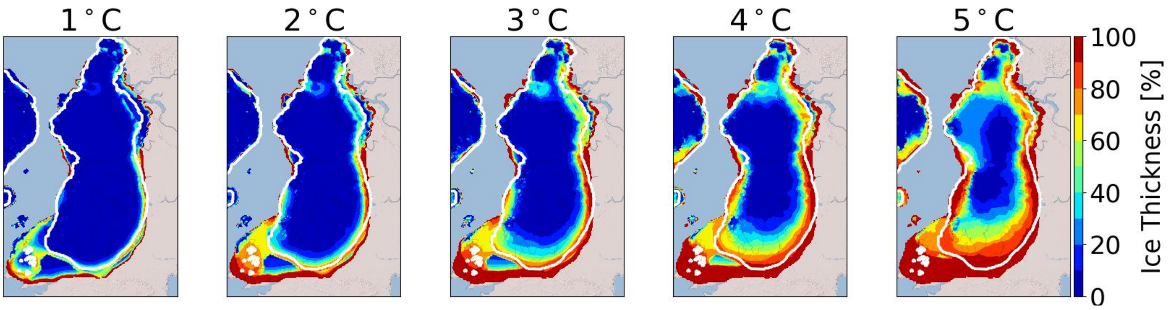

Figure 7: Multi-model mean of the ice thickness lost after 1000 GRISLI model years in the EXP1 experiments with respect to the ice thickness of the LGM ice sheet (red: 100% lost). The results are plotted on the largest ice

sheet mask. The white line corresponds to the common ice sheet mask of the five models, i.e., where the multi-model mean is computed on the 5 models.

To better understand the effect of precipitation on the EIS stability, the EXP2 combines the precipitation and surface air temperature perturbations. The results obtained in the EXP2 experiments are shown in figure SP4. For BIIS and FIS, a similar behavior to EXP1 is observed, albeit with less ice melt due to increased accumulation as a result of increased temperatures. On the contrary, in EXP2, a large difference with EXP1 is simulated for BKIS, where only the ice sheet margins show sensitivity to increased temperature and precipitation. While an inland ice loss between 20% and 50% was simulated in EXP1 in some places, it is generally limited to less than 10% in EXP2. This result shows the significant role of precipitation to counteract the ice loss due to an increase in surface air temperature.

4.2.2 EXP3: Basal melting

Besides changes in SMB, another factor that can destabilize a marine ice sheet is the basal melting under the ice shelves (Pritchard et al., 2012). In the LGM experiments, the numerical Kt value is fixed to 7 m °C^{-1} yr^{-1} and leads to basal melting rates in the BJR and SA sectors of 3.1 m yr^{-1} and 0.7 m yr^{-1} respectively. To investigate the effect of increased basal melting that likely occurred during the last deglaciation as a response of increased ocean temperatures, we performed sensitivity experiments by first changing the Kt value (EXP3.1). The sensitivity to oceanic temperatures (EXP3.2) will be discussed later.

Figure 8 displays the percentage of ice thickness losses (with respect to the initial configuration) for Kt ranging from 10 m °C^{-1} yr^{-1} to 50 m °C^{-1} yr^{-1}. After 1000 years of simulation, no change in ice thickness is observed for Kt = 10 m°C^{-1} yr^{-1}. For higher Kt values (15 m °C^{-1} yr^{-1} and 25 m °C^{-1} yr^{-1}), ice losses between 30% to 40% are simulated in the MN ice stream sector, and 100% of the ice shelf in the south of SA sector is melted (see Fig 3 showing the presence of ice shelves at the end of the spin-up experiment). This corresponds to basal melting rates (multi-model mean) near the grounding line ranging from 7.5 m yr^{-1} (Kt = 15 m °C^{-1} yr^{-1}) to 10.4 m yr^{-1} (Kt = 25 m °C^{-1} yr^{-1}) in the MN sector and from 1.7 m yr^{-1} (Kt = 15 m °C^{-1} yr^{-1}) to 2.9 m yr^{-1} (Kt = 25 m °C^{-1} yr^{-1}) in the SA sector. However, these changes are restricted to small areas, and the ice loss is not significant enough to firmly indicate a noticeable sensitivity to basal melting. Perturbations with Kt values above 25 m °C^{-1} yr^{-1} are necessary to observe significant changes in the EIS configuration. In particular, for Kt = 50 m °C^{-1} yr^{-1}, the ice is entirely melted near the BIIS margins, and less than 50 % of the ice remains in the regions of MN, SA and BJR ice streams. Nonetheless, only the simulations forced by MPI-ESM-P, MPI-ESM1.2 and MIROC-ESM show a sensitivity to basal melting in BJR, MN and SA sectors (Fig. SP5). Depending on the GCM forcing, the simulated basal melting values range between 25.7 and 28.7 m yr^{-1}, 24.4 and 28.2 m yr^{-1} and between 11.2 and 13.4 m yr^{-1} for the BJR, MN and SA sectors respectively. By contrast, very small values are obtained with IPSL-CM5A2 (0.2 m yr^{-1} 0.5 m yr^{-1}) and IPSL-CM5A-LR models (0.5 m yr^{-1}). This can be explained by the cold oceanic temperatures near the BJR sector compared to those simulated by the three other GCMs (Fig SP6). These results show that the basal melting has the ability to destabilize the BKIS when it exceeds a certain threshold. Results inferred from the simulations forced by MPI-ESM-P, MPI-ESM1.2 and MIROC-ESM suggest that this threshold is obtained for Kt values between 25 and 50 m °C^{-1} yr^{-1}, corresponding to basal melting rates at the grounding line between 10.4 m yr^{-1} and 28.7 m yr^{-1} for the BJR sector and between 6.2 and 13.4 m yr^{-1} for the SA sector. By comparison, a basal melting rate of 22 m yr^{-1} has been observed thanks to radar measurements in the mouth of the Mercer/Whillans Ice

Stream located in the West Antarctic ice sheet (Marsh et al., 2016). Providing that Kt values are greater than 25 m°C^{-1} yr^{-1} (or close to 50 m °C-1 yr^{-1}), the region of the BJR ice stream responds to basal melting perturbations with basal melting rates similar to those observed in some parts of WAIS. However, the ice loss is restricted to the very edge of the ice sheet and the BKIS retreat is negligible. This raises the question as to whether the basal melting exerts a stronger influence on longer time scales. Therefore, we also investigated the ice sheet behavior after 10 000 model years.

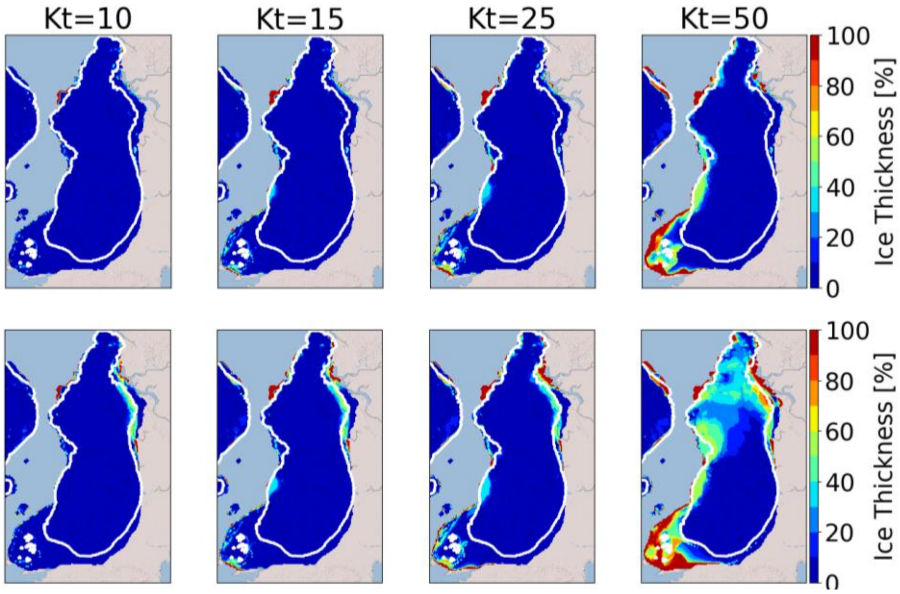

Figure 8: Multi-model mean of the ice thickness lost after 1000 (top) and 10 000 (bottom) GRISLI model years in the EXP3.1 experiments with respect to the ice thickness of the LGM ice sheet. (red: 100% lost). The white line corresponds to the common ice sheet mask of the five models, i.e., where the multi-model mean is computed on the 5 models. Kt is the transfert factor in Eq 6, express in m yr^{-1} °C^{-1}.

A similar behavior is observed after 10 000 years for Kt between 10 and 25 m °C^{-1} yr^{-1}, with the exception of the southern part of BKIS bordering the Kara Sea where a 30% to 50% ice thickness decrease, with respect to the initial one, is obtained. For Kt=50 m °C^{-1} yr^{-1}, more than 40% of ice loss is simulated for BKIS, and up to 60% in the BJR sector. As previously mentioned, this large ice thickness decrease in the center of BKIS is highly GCM-dependent, and is only observed in simulations forced by the MIROC and MPI models (Fig. SP5

As the basal melting parameterization is expressed as a quadratic function of the oceanic temperatures, we may expect a different sensitivity of EIS when the oceanic temperatures increase (EXP3.2). Results of the EXP3.2 experiments are shown in figure SP7. Perturbations of oceanic temperatures between +0.5°C and +1.5°C lead to basal melting rates at the grounding line of the BJR sector of less than 3.8 m yr^{-1}. This is well below the threshold suggested by the results of the EXP3.1 experiments (between 10.4 and 30 m yr^{-1}), and no significant ice loss is simulated after 10 000 years of simulation.

For larger perturbations (+7.5°C and +10°C), larger values of the basal melting rates are obtained in the BJR (11.6 and 17.5 m yr^{-1}), in the SA (10.8 and 15.6 m yr^{-1}) and in the MN sectors (11.5 and 17.4 m yr^{-1}) after 10 000 model years. A perturbation of 7.5°C does not trigger the ice retreat because of a too low basal melting. By contrast, when the perturbation reaches +10°C, a similar behavior to that simulated with Kt=50 m °C^{-1} yr^{-1} (EXP3.1) is obtained.

On the other hand, for simulations forced by IPSL-CM5A2 and IPSL-CM5A-LR, an increase in oceanic temperatures of +10°C allows us to observe a sensitivity of BKIS in the SA sector (see Fig SP8) after 1000 years of simulations, which leads to a total retreat of the eastern part of BKIS after 10000 years.

These results show that the BJR, MN and SA regions are sensitive to sub-shelf melting providing that the basal melt exceeds a certain threshold obtained for Kt values greater than 25 m $°C^{-1}$ yr^{-1} (and greater than 10 $m°C^{-1}yr^{-1}$ for the MN sector) or for a rise in oceanic temperature greater than 7.5°C. From the combination of EXP3.1 and EXP3.2 experiments, it appears that the threshold is between 11.6 m yr^{-1} and 17.5 m yr^{-1} for the BJR sector, between 6.2 and 13.4 m yr^{-1} for the SA sector and lower than 7.5 m yr^{-1} for the MN sector. Moreover, our results also suggest that the large retreat of one single ice stream has the ability to favor the total retreat of the whole of BKIS

4.2.3 EXP4: Combined effects of basal melting and surface air temperatures

Results presented in the previous section suggest that sub-shelf melting has only a poor impact on the EIS destabilization for Kt perturbations below a certain threshold estimated to lie between 25 and 50 m $°C^{-1}$ yr^{-1}, or below a + 10°C increase of oceanic temperatures. However, increases in surface melting due to atmospheric warming may lead to changes in the geometry of the grounded ice sheet and floating ice shelves. In turn, changes in the EIS configuration may alter the EIS sensitivity to basal melting. To test this hypothesis, we combined surface air temperature perturbations with basal melting perturbations (EXP4) and compared the results with those of the EXP1 experiments. Figure 9 displays the difference in the total BKIS ice volume after 1000 years between EXP4 and EXP1 experiments ($\Delta V_{4\text{-}1}$) for different surface atmospheric temperature perturbations (ΔT = +2°C, +3°C and +4°C) and Kt values fixed to 25 and 50 m $°C^{-1}$ yr^{-1} (negatives values are associated to a greater ice loss in EXP4 than in EXP1). For both Kt perturbations (Kt = 25 and 50 m $°C^{-1}$ yr^{-1}), no significant difference in the ΔV_{4_1} values (computed for the different ΔT perturbations) is observed in simulations forced by IPSL-CM5A2 and IPSL-CM5A-LR. This illustrates the poor sensitivity of BKIS to basal melting with the IPSL climate forcings. As explained in section 4.2.2, this low sensitivity is due to the cold oceanic temperatures simulated in both IPSL models (see Fig. SP6). For the three other simulations (forced by MIROC-ESM, MPI-ESM-P, and MPI-ESM1.2), the ice volume difference is clearly amplified with higher ΔT levels, especially when the Kt transfer coefficient is higher. For example, for Kt=50 $m°C^{-1}yr^{-1}$, the difference in ΔV_{4_1} values between the initial ice sheet configuration (ΔT = 0°C) and ΔT = 4°C is ~60 000 km^3 with MPI-ESM-P, against ~20 000 km^3 when Kt=50 $m°C^{-1}yr^{-}1$. A similar behavior is observed for simulations forced by MIROC-ESM (~110 000 km^3) and MPI-ESM1.2 (~60 000 km^3). To better illustrate the impact of the combination of both temperature and basal melting perturbations, we plotted the evolution of ice loss every 1kyr as simulated in the EXP1 (ΔT = +4°C), EXP3 (Kt=50 $m°C^{-1}yr^{-1}$) and EXP4 experiments in figures SP9 to SP11. For the simulation forced by MIROC-ESM (Fig. SP11), the largest part of the deglaciation signal is dominated by increased atmospheric temperatures in the EXP4 (see Fig SP11). Simulations forced by MPI-ESM-P and MPI-ESM1.2 have a different behaviour (Figs SP9 and SP10) and show a significant difference between EXP1 and EXP4 and between EXP3 and EXP4. In the EXP3 experiment, the SA sector appears to be highly sensitive, mainly due to high ocean temperatures (> 3°C, see fig SP6) in contrast to the BJR sector where only a part has deglaciated after 10 000 years. However, in the EXP4 experiment, in which near-surface temperature and basal melting are combined, BKIS starts to retreat after 1000 years and has almost entirely melted after 10 000 years. This suggests that the BKIS deglaciation is initially triggered by surface warming but is further amplified by basal melting.

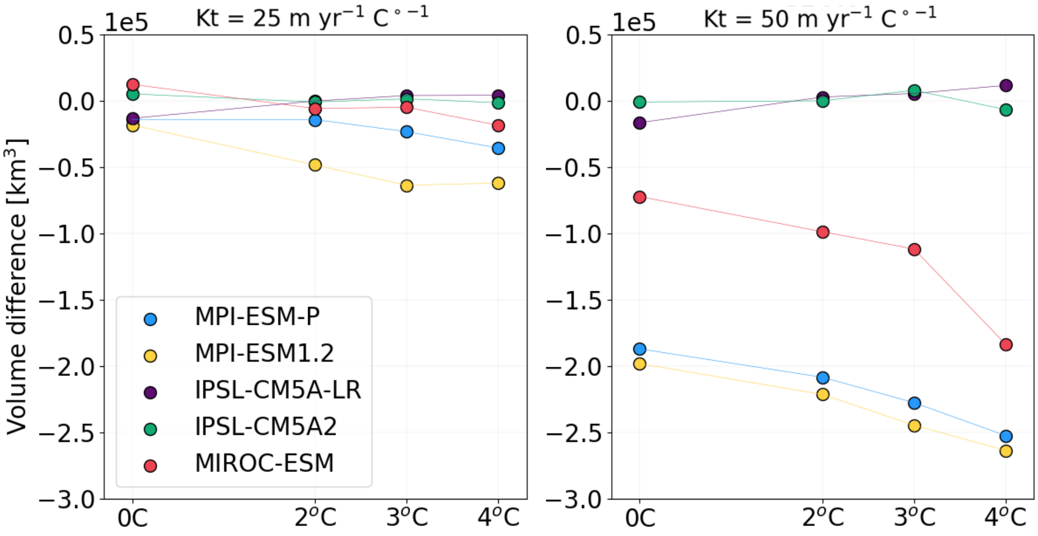

Figure 9: Differences of the ice volume lost between EXP4 and EXP1 (ΔV_{4-1}) after 1000 years for Kt=25 m °C^{-1} yr^{-1} (left) and Kt=50 m °C^{-1} yr^{-1} (right).

4.2.5 Exp5: Sea level

In the previous simulations, the sea level forcing was fixed to -120 m (with respect to the present-day eustatic sea level), corresponding to the estimated eustatic level at the LGM (Peltier et al., 2002). In this series of experiments, we quantify the sensitivity of the EIS to different sea level forcings.

The multi-model mean difference between the ice thickness after 1000 GRISLI model years and the initial ice thickness (sea level = -120 m) is displayed in Figure 10 for the different sea level elevations ranging from -115 m to 0 m. After 1000 years of simulation, for sea levels ranging from -115 m to -105 m, no significant differences are observed with respect to the reference simulation (i.e., - 120 m). For larger perturbations, the MNIS sector appears to be the most sensitive. As an example, for a sea level of – 90 m, an ice loss of ~40 % is simulated in this area, and an almost complete retreat is obtained for a sea level higher than -60m, with an ice thickness decrease of up to 80%-100%. Although sea level elevations of -90 m and – 60 m are considerably larger than the global mean sea level at the LGM, they are consistent with the local sea level variations that could be as high as -70 m as suggested by Gowan et al. (2021). However, for the other sectors (BJR, SA, NCIS), ice thickness decrease is only obtained for sea levels higher than -30 m which is largely out of the range advanced by Gowan et al. (2021). As a result, this series of experiments conducted with the GRISLI model suggests that the elevation of sea level has only played a marginal role at the beginning of the EIS deglaciation.

However, it should be noted that sea level rise can lead to changes in the geometry of the ice sheet and floating ice shelves. Therefore, these changes in the EIS configuration may influence its sensitivity to oceanic temperature perturbations. We tested this hypothesis by raising the sea level from -120 m to -110 m compared to the current level and by raising concomitantly the oceanic temperatures (+1.5°C and +10°C). Adding a sea level perturbation to the oceanic temperature perturbation does not drastically change the response of the ice sheet. Differences of 6 to 7 % in ice volume losses were only observed for the highest temperature perturbation (+10°C) after 10 000 years for only two GCM forcings (MIROC-ESM and IPSL-CM5A2), while the differences are negligible (lower than 2%) for smaller perturbations, shorter timescales and other GCM forcings (not shown).

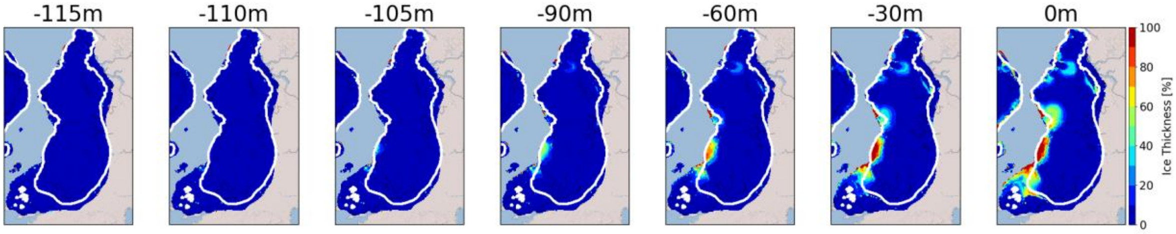

Figure 10: Multi-model mean of the ice thickness lost after 1000 model years in the EXP5 with respect to the ice thickness of the LGM ice sheet. (red: 100% lost). The white line corresponds to the common ice sheet mask of the five models, i.e., where the multi-model mean is computed on the 5 models.

4.3 Sensitivity to the spin up method

The construction of spin-up is one of the most important factors impacting the sensitivity of the EIS. The LGM ice sheets presented in Section 4.1 were constructed under a constant LGM climate during 100 000 years. The specificity of this method is to construct ice sheets in good equilibrium with their environment. However, as outlined by Batchelor et al. (2019), the EIS was far from being in equilibrium with the climate at the LGM.

In order to look into the biases associated with the choice of the spin-up method, we compared the results obtained with a transient spin-up procedure. For this purpose, we reconstructed a climatology evolving from the Last Interglacial (-127 000 years) to the LGM (-21 000 years). The transition between these two climatic states is obtained by using a multi-proxy following the same method as Quiquet et al. (2013). For the period between -127ka and -122ka, we used an index based on SST reconstructions (McManus et al., 1999; Oppo et al., 2006) and from -122ka to -21ka we chose an index based on North GRIP δ^{18}O (North GRIP members, 2004). In the same way as above, we used the 10 PMIP3/PMIP4 forcings shown in Table 1. As the last interglacial simulations were not available for some of the PMIP3/PMIP4 models, we made the approximation that the -127 000 climate was represented by the pre-industrial climate (i.e. piControl experiments, Eyring et al., 2016).

At the end of the of these new spin-up simulations, only 4 PMIP forcings (MPI-ESM-P, MPI-ESM1.2, IPSL-CM5A2 and IPSL-CM5A-LR) succeeding in constructing the EIS in agreement with the reconstructions (see figure SP12h). Compared to previous LGM ice sheets presented in Section 4.1, the ice extent is smaller (Fig. SP12h) and the dome of FIS is flatter with sharper edges. Furthermore, contrary to the previous method of spin-up construction (i.e. constant LGM forcing), the simulation forced by MIROC-ESM failed to form an ice sheet over the Barents Sea.

To assess the effect of the LGM EIS obtained after each of the transient spin-up experiment obtained with MPI-ESM-P, MPI-ESM1.2, IPSL-CM5A2 and IPSL-CM5A-LR, we applied atmospheric temperature perturbations (+1°C and +5°C, as in EXP1) and basal melting perturbations (Kt values of 10 m°C^{-1}yr^{-1} and 50 m°C^{-1}yr^{-1}, as in EXP3.1). Finally, we compare the percentage of remaining ice volume with the reference one (i.e simulated in EXP1 and EXP3.1) and the new perturbed simulations after 1000 and 10 000 years using the following formula:

$$\delta = \frac{V_{pert}(t{=}end) - V_{pert}(t{=}0)}{V_{pert}(t{=}0)} - \frac{V_{ref}(t{=}end) - V_{ref}(t{=}0)}{V_{ref}(t{=}0)} \quad (8)$$

Each term in the right-hand side of Equation (8) represents the percentage of ice volume loss in a given simulation. δ represents the difference (in %) of ice volume loss between the new simulation and the reference simulation, with V_{pert} being the ice volume for the new perturbed simulation (transient spin-up) and V_{ref} the ice volume of the EXP1 and EXP3 simulations. A negative value of V_{ice} indicates a greater retreat of EIS of the new EIS configurations (i.e. obtained with the transient spin-up method).

Figure 11a shows the results of the computed δ value (see Eq. 8) after 1000 (left) and 10 000 model years (right) averaged over all models for atmospheric (1°C and 5°C) and oceanic (Kt = 10 and 50 m°C^{-1}yr^{-1}) perturbations. After 1000 years, no significant difference is observed between both simulations. Conversely, after 10 000 years, a difference of the order of -10% for perturbations of 1°C and 10 m°C^{-1}yr^{-1} is observed. This can be explained by internal processes that are not in equilibrium with the LGM climate at the end of the transient spin-up simulation. More specifically, large differences in the simulated effective pressure are obtained at the end of both spin-up experiments. In the reference spin-up simulation (constant LGM climate), there is a relatively low effective pressure since sub-glacial water has accumulated over the 100 000 year of simulation (Fig. SP13). By contrast, in the spin-up constructed by the transient method, large parts of the ice sheet are englacial for much shorter time periods with smaller amount of sub-glacial water resulting in higher effective pressure. This leads to drastically different sliding velocities among the two spin-up methods, with much smaller ice sheet velocities after the transient spin-up. During the perturbation experiments, the sub-glacial water tends to accumulate when using the transient spin-up ice sheet state. The temporal evolution in this case reflects the decrease in the effective pressure (and related increase in velocity) on top of the applied atmospheric or oceanic perturbation. The sensitivity over time scales greater than one thousand years in these new experiments is thus not directly comparable to the reference sensitivity experiments in which the effective pressure is fully equilibrated.

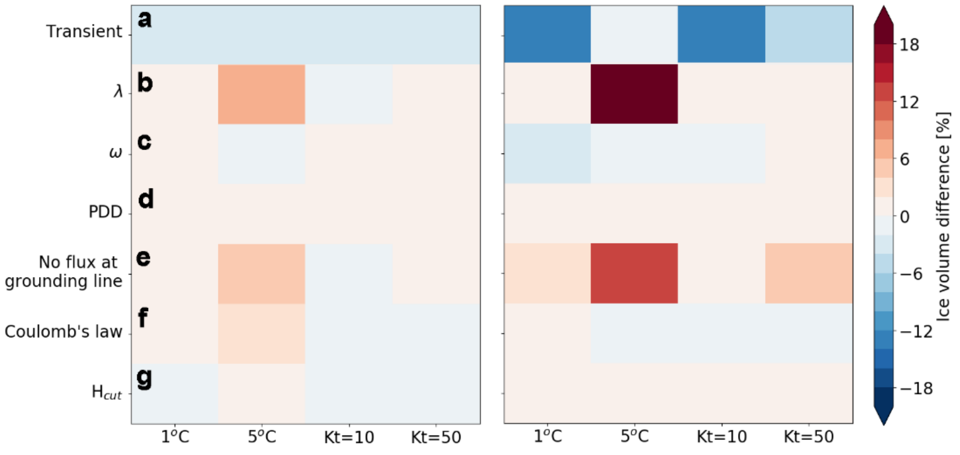

Figure 11: Multi model mean of the differences in ice volume loss between the new perturbed simulations and the reference simulations (EXP1 and EXP3) after 1000 years (left) and after 10000 years (right). Note that the multi model mean is done without the contribution of MIROC-ESM forcing for the panel a. The volume difference is calculated thanks to the equation 8. λ is the vertical temperature gradient, ω is the ratio precipitation/temperature change and H_{cut} is the calving criterion. More information is disponible in table 4.

4.4 Sensitivity to different GRISLI configurations

The results presented in Section 4.2 suggest that the EIS was primarily sensitive to atmospheric forcing at the beginning of the last deglaciation. However, we cannot exclude that this finding is specific to the choices of model parameters (Table 2) and physical parameterizations (Table 3). In order to assess the extent to which the observed EIS sensitivity is driven by these choices, we conducted additional experiments with alternative values of climate-related parameters (vertical temperature gradient, the precipitation ratio to temperature change, degree-day factors in the PDD formulation). We also changed the basal friction law and removed the parameterization of the ice flux at the grounding line (Table 4). We first performed 100 000-year simulations using the same procedure as for the reference simulations (Fig. SP12a-g). Note that the CNRM-CM5, GISS-E2-R, MIROC-ES2L, FGOALS-G2 and MRI-CGM3 fail to reproduce an ice sheet in agreement with the reconstructions similarly to as our reference experiments (see Sections 4.1 and 4.2).

Next, we applied atmospheric temperature perturbations (+1°C and +5°C) and basal melting perturbations (Kt = 10 m°C^{-1}yr^{-1} and 50 m°C^{-1}yr^{-1}) to evaluate the relative importance of both atmospheric and oceanic forcings with the modified GRISLI configurations.

Table 4: List of sensitivity experiments (columns 5-10) performed with changes in the standard GRISLI configuration. New values of model parameters are given in column 4 with reference values indicated in parentheses. Changes in physical parametrizations are indicated in column 2.

exp	**GRISLI configuration changes**			**Spin-up methods**		**Perturbations experiments**			
n°	**Variables**	**Name**	**Value**	**Constant LGM**	**Transient**	**1°C**	**5°C**	**Kt=10**	**Kt=50**
1	Spin-up method	-	Transient		✓	✓	✓	✓	✓
2	Vertical temp gradient	λ	4 °C km^{-1} (*7*)	✓		✓	✓	✓	✓
3	Precip/temperature change	ω	0.05 °C^{-1} (*0.11*)	✓		✓	✓	✓	✓
4	PDD coefficients	$\mathrm{C}_{\mathrm{ice,snow}}$	- 25%	✓			✓	✓	✓
5	PDD coefficients	$\mathrm{C}_{\mathrm{ice,snow}}$	+ 25%	✓		✓			
6	Flux at the grounding line	-	None	✓		✓	✓	✓	✓
7	Basal friction law	-	Plastic drag	✓		✓	✓	✓	✓
8	calving criterion	H_{cut}	50 m (*250*)	✓		✓	✓	✓	✓

4.4.1 Sensitivity to climate parameters

At first, we examined the sensitivity of EIS to a vertical temperature gradient of 4 °C km^{-1} (instead of 7 °C km^{-1}) which is considered by Marshall et al. (2007) as the most likely value of the near-surface temperature lapse rate. Therefore, a decrease in ice thickness of 100 meters results in a decrease in atmospheric temperature of 0.4 °C instead of 0.7 °C (see Eq. 4). This choice aims at reducing the sensitivity of EIS to atmospheric forcing in order to analyze whether the ice sheet is more responsive to the oceanic forcing.

Secondly, in EXP2, we found that increased precipitation as a result of increased temperatures (see Eq. 5) tends to reduce the sensitivity of EIS. In the reference simulations (Section 4.2), the precipitation ratio to temperature change (ω value) was set to 0.11°C^{-1}. However, lower values can be found in the literature ranging between 0.05 °C^{-1} and 0.11 °C^{-1} (Petrini et al., 2020, Charbit et al., 2013, Quiquet et al., 2013). We therefore investigated whether the choice of a lower precipitation-temperature ratio, which is expected to lower the precipitation dependency to temperatures, could influence the response of the EIS. In this new series of sensitivity experiments, the ω parameter was fixed to 0.05 °C^{-1}. In doing so, our objective is to assess whether a variation in ω can lead to significant changes in the response of the ice sheet to atmospheric forcing.

At last, Charbit et al. (2013) demonstrated that that the choice of the PDD formulation can have a substantial impact on the computed amount of ice melt. In order to assess the impact on the stability of the EIS of the melt coefficient Cice and Csnow, as defined in Tarasov and Peltier (2002), we decreased (resp. increased) their values by 25% for the +5°C (resp. +1°C) temperature perturbation. Decreasing (resp. increasing) the melt coefficients by 25% for the temperature perturbations allows to reduce (resp. increase) the influence of the atmospheric forcing on the evolution of the EIS. In addition, in order to reduce the influence of the surface air temperatures, we have also tested the impact of decreased melt coefficients in the basal melting perturbation experiments.

The results of these new sensitivity experiments are analyzed in terms of differences in ice volume loss at years 1000 and 10 000 years with the reference simulations (δ value, see Eq. 8) and are displayed in figure 11 (b-d). The only significant differences with the reference simulations are obtained for a 5°C perturbation due to a lowered temperature-elevation feedback in the simulation with $\lambda = 0.4$ °C km^{-1}. For all the other experiments changes in the ω parameter or in the degree-day factors, differences with reference simulations are less than $\pm$ 2%. As such, this series of perturbed experiments shows that changing climate-related model parameters results in only small changes in the EIS ice volume loss compared to the standard configuration of the GRISLI ice-sheet model, and does not question the prevailing influence of the atmospheric forcing suggested by our reference sensitivity experiments.

4.4.2 Sensitivity to physical parameterizations

Besides the climate related parameters, changes in the representation of the dynamic processes may have a strong impact on the relative importance of the mechanisms responsible for the triggering of the EIS retreat. For example, using the PSU ice sheet model (Pollard and De Conto, 2012), Petrini et al. (2018) found that the implementation of a grounding line flux adjustment reduces the sensitivity of BKIS. To go a step further and compare our findings with those of Petrini et al. (2018), we removed the grounding line flux parameterization in the GRISLI model and assessed its impact on the EIS sensitivity. Without the flux adjustment, the EIS sensitivity to basal melting and atmospheric temperature perturbations is reduced (Fig. 11e). This contrasts with the findings of Petrini et al (2018). More specifically, after 10 000 years, a + 5°C atmospheric perturbation results in a reduced amount of melting of about 14% compared to the reference experiment (with parameterization of the grounding line flux). In other words, these results suggest that in the absence of the grounding line flux adjustment, higher atmospheric temperatures can potentially enhance the ice sheet's sensitivity to oceanic forcing through grounding line retreat.

Another source of huge uncertainties lies in the choice of the basal friction law (e.g. Brondex et al., 2017, Joughin et al., 2019; Akesson et al., 2021). An appropriate choice of this law is of primary importance as basal friction exerts a strong control on the dynamics of the grounding line and fast-flowing ice streams. In our previous experiments, the basal friction was parameterized using a linear dragging law (Eq. 2). In order to investigate the extent to which the choice of the friction law can influence the sensitivity of the EIS to atmospheric temperature and basal melting perturbations we used a plastic dragging law where the basal drag depends quadratically on the basal velocity (Pattyn et al., 2017).

In contrast to previous works investigating the ice sheet sensitivity to friction laws, our findings reveal that experiments using the non-linear basal friction do not exhibit significant differences compared to EXP1 and EXP3 simulations after 1,000 and 10,000 years (Fig. 11f). However, it is important to note that Joughin et al. (2019) and Akesson et al. (2021) explored the sensitivity of the Antarctic ice sheet, which differs from the EIS configuration. This may explain (at least partly) why the EIS may exhibits a different sensitivity to changes in the friction law.

Thinning of confined ice shelves through basal melting produce a weakening of the buttressing effect, implying an acceleration of the grounded ice streams and ultimately a substantial ice discharge in the ocean. This sequence of events was observed in the Antarctic Peninsula after the collapse of the Larsen B Ice Shelf in 2002 (Rignot et al., 2004; De Rydt et al., 2015). In our reference experiments, the ice shelf extent is small (Fig. 3). This likely explains why the EIS appears poorly sensitive to basal melting. In order to potentially increase the area of ice shelves, we reduced the calving criterion from 250 m to 50 m. This results in a slight increase of the ice shelf area at the LGM (Fig. SP12d) compared to the reference simulations (Fig 3). However, this increase did not result in a substantial change of the sensitivity of the EIS to basal melt and atmospheric temperature perturbations (Fig. 11g). This limitation is due to the topography, which does not allow for adequate confined ice shelf development, unlike the Antarctic, where the presence of bays (in Ross and Weddell Seas for example) allows the formation of confined ice shelves.

Thus; as previously highlighted for the GRISLI climate-related parameters, changing the parameterizations related to ice dynamics does not modify the main conclusion related to the dominating effect of the atmospheric forcing compared to the oceanic forcing.

5. Discussion

As in Niu et al. (2019), the results of our experiments suggest that the EIS ice sheet is very sensitive to the atmospheric warming that may have occurred at the beginning of the last deglaciation. By contrast, basal melting does not seem to be a key process for triggering the ice sheet retreat. However, once the atmospheric warming has initiated the retreat, basal melting has the capability of accelerating the retreat, as supported by the results of EXP4, providing that the amount of basal melting is high enough. Nevertheless, these conclusions are strongly dependent on the ice-shelf configurations. Indeed, unconfined ice shelves do not exert an efficient buttressing effect (i.e., the stress that the ice shelves exert at the grounding line) and their removal has almost no impact on the dynamics of the grounded ice sheet (Gundmundsson et al., 2013, Fürst et al., 2016).

The small sensitivity to the oceanic forcing simulated in the EXP3 experiments contradicts the conclusions of previous modeling studies of the EIS behavior during the last glacial period (Alvarez-Solas et al., 2019) and the last deglaciation (Petrini et al., 2020). Both conclude that oceanic temperatures are the main driver of the EIS destabilization. Their findings are all the more surprising as they both use an ice-sheet model (GRISLI1.0) similar to ours (GRISLI2.0). However, several differences can be noticed between their modeling approach and that of the present study. First, GRISLI1.0 does not include a parameterization of the ice flux at the grounding line. Therefore, it should be easier with our model to trigger the EIS retreat through basal melting because GRISLI2.0 includes key processes to simulate the marine ice sheet instability. To verify this issue, we performed additional simulations similar to the EXP3 ones by removing the grounding line flux parameterization, and as expected, results clearly show that the removal of this parameterization limits the ice loss (not shown). One of the most likely explanation of the disagreement between our findings and those of previous studies (Alvarez-Solas et al., 2019; Petrini et al., 2020) relies on the procedure followed in the spin-up experiments. Both built their initial state in the same way. To favor the EIS build-up, they fixed the basal melting to 0.1 m yr^{-1} during their ice sheet spin-up. Starting from the EIS configuration obtained at the end of the sign-up experiment, they used a linear (Alvarez-Solas et al., 2019) or quadratic (Petrini et al., 2020) basal melting parameterization depending on the oceanic temperature to simulate the last glacial period (Alvarez-Solas et al., 2019) or the last deglaciation (Petrini et al., 2020) of EIS. In doing so, there is a methodological inconsistency between the spin-up simulation and the subsequent experiments. To investigate the effect of such inconsistency on the EIS deglaciation, we followed their spin-up methodology (homogeneous basal melting) instead of the one described in Section 2.3. The resulting LGM ice sheets resemble those presented in Sec. 3.1, except that the MIROC-ESM forcing produces large ice shelves in the Greenland and Norwegian seas. We then applied the same perturbations as in EXP3 on these alternative ice sheets with a basal melting parameterization depending on the oceanic temperature and salinity (see Eq7). We display in Figure 12 the percentage of ice thickness lost after 10000 years with respect to the initial configuration for Kt ranging from 15 to 50 m °C^{-1} yr^{-1} for this new series of experiments. Compared to EXP3, we show that the EIS now presents a much more significant sensitivity in the BIIS and FIS for a perturbation of Kt=50 m °C^{-1} yr^{-1}. These results illustrate the extent to which the conclusions drawn for the driving mechanisms of the EIS destabilization strongly depend on the initial state. However, we argue that the approach followed in the present paper is more consistent as the basal melting parameterization is exactly the same for the spin-up procedure and the sensitivity experiments.

Another difference that deserves to be mentioned is that Petrini et al, (2020) used a climatic index based on the transient simulation of Liu et al., (2009). This method ensures that both the atmospheric and oceanic temperatures increase concomitantly up to their pre-industrial levels. As a result, we cannot exclude that the key role of basal melting in their simulated deglaciation is not amplified by the effect of atmospheric warming, similarly to the conclusions drawn from our EXP4 results.

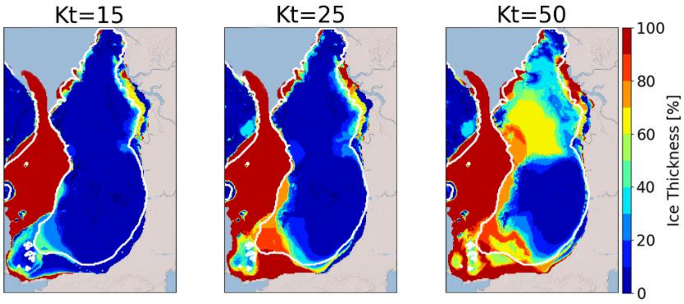

Figure 12: Multi-model mean of the ice thickness loss compared to the initial ice sheet for different basal melting perturbations. LGM ice sheets are built by fixing the basal melting to 0.1 m yr^{-1} (as in Petrini et al., 2020; Alvarez-Solas et al., 2019). Note that the significant decrease in ice thickness in the Norwegian and Greenland seas is due to the simulation of ice shelves in the new spin-up for the MIROC-ESM forcing (see Fig. SP13). These ice shelves are extremely sensitive to a change in the basal melt. The white line indicates the areas where the multi-model mean is done on the 5 models. Kt is the transfert factor in Eq 6, express in m yr^{-1} $°C^{-1}$.

The second round of sensitivity experiments conducted with new values of climate-related parameters and new parameterizations related to the ice dynamics also confirm the high sensitivity of the EIS to the atmospheric forcing in the GRISLI ice sheet model. This contrasts with the current situation in the West Antarctic Ice Sheet (WAIS), where ice volume loss is mainly due to melting under the ice shelves (Pritchard et al., 2012). This difference in the response of the two ice sheets raises questions about the mechanisms responsible for their respective evolution.

In addition, WAIS is characterized by large areas of confined ice shelves exerting a buttressing effect on the grounded ice, whereas most of the ice shelves in our simulated LGM EIS are unconfined (see Section 4.4.2) However, as temperatures are expected to rise in the future, larger amounts of meltwater will be produced on the surface of the ice shelves (Kittel et al., 2021), favouring potentially the ice-shelf disintegration through hydrofracturing (Banwell et al., 2013; Lai et al., 2020). Although this process differs from basal melting, it could bring WAIS into a similar configuration to the past Eurasian ice sheet.

The ISMIP6 project (Seroussi et al., 2020) shows a significant difference in ice sheet behavior depending on the ice sheet model used (Seroussi et al., 2020). Despite the numerous sensitivity experiments presented in this study with various parameter values and different parameterizations of the ice dynamics (see section 4.4), we cannot totally exclude the possible model-dependency of our results To reduce the uncertainties associated with the use of a single ice sheet model, we strongly encourage other ice-sheet modelers to perform the same kind of sensitivity tests with several other ice sheet models having, if possible, higher resolution so as to better capture the fine-scale structure of outlet glaciers and the ice flow dynamics at the grounding line and the marine ice sheet instability.

6. Conclusion

In this paper, we used off-line GRISLI2.0 simulations forced by PMIP3/PMIP4 models to investigate the key mechanisms driving the retreat of the Eurasian ice complex at the beginning of the last deglaciation. We gave a special attention to the understanding of the processes responsible for the destabilization of the marine-based parts of the Eurasian ice sheets as GRISLI2.0 includes and explicit calculation of the ice flux at the grounding line which is expected to account for the representation of the marine ice sheet instability. We first showed that, due to too strong climate biases in some GCMs at the LGM, only 5 out of 10 GCMs succeeded in building an ice sheet in agreement with the reconstructions.

The sensitivity experiments have been designed to test the response of the simulated Eurasian ice sheets to surface climate, oceanic temperature and sea level perturbations. Our results highlight the high EIS sensitivity to a change in surface atmospheric temperatures using the GRISLI model. While basal melting does not seem to be the main driver of the ice sheet retreat, we showed that its effect is clearly amplified by the atmospheric warming.

These results contradict those of previous studies mentioning the central role of the ocean on the deglaciation of BKIS. However, we argue that parts of this disagreement are related to the way the climatic forcing is done (absolute climatic fields, anomalies or climatic indexes) and the procedure followed for building the initial state of EIS and to the presence of confined or unconfined ice shelves at the LGM. In order to assess the robustness of our analyses, we suggest to other modelling groups to reproduce the same kind of sensitivity tests with ice sheet models of similar or higher complexity. This pluralistic approach would allow to better understand the uncertainties associated with the ice sheet model used.

Data availability. The source data of the experiments presented in the main text of the paper are available on the Zenodo repository with the digital object identifier https://doi.org/10.5281/zenodo.7528183 (van Aalderen et al, 2023).

Code availability. The GRISLI2.0 code is available upon request from Aurelien Quiquet (aurelien.quiquet@lsce.ipsl.fr) and Christophe Dumas (christophe.dumas@lsce.ipsl.fr) (Laboratoire des Sciences du Climat et de l'Environnement (LSCE)).

Author contributions. All authors designed the study. VVA performed the numerical experiments. All authors contributed to the analysis of model results. VVA and SC wrote the manuscript with inputs from CD and AQ.

Competing interests. The authors declare that they have no conflict of interest

Acknowledgements. The authors are very grateful to Irina Rogozhina who edited the manuscript as well as E. Gowan and two anonymous reviewers for their constructive comments that greatly help improve the manuscript. Victor van Aalderen is funded by the French National Research Agency (Grant: ANR-19-CE01-15). We acknowledge the World Climate Research Programme's Working Group on Coupled Modelling, which is responsible for the Paleoclimate Modelling Intercomparison Project (PMIP) and we thank the climate modeling groups (listed in Table 1 of this paper) for producing and making available their model outputs. This work benefited from productive exchanges with NicolasJourdain and Didier Swingedouw.

References

Abe-Ouchi, A., Saito, F., Kageyama, M., Braconnot, P., Harrison, S. P., Lambeck, K., Otto-Bliesner, B. L., Peltier, W. R., Tarasov, L., Peterschmitt, J.-Y., and Takahashi, K.: Ice-sheet configuration in the CMIP5/PMIP3 Last Glacial Maximum experiments, Geosci. Model Dev., 8, 3621–3637, https://doi.org/10.5194/gmd-8-3621-2015, 2015.

Adloff, M., Reick, C. H., and Claussen, M.: Earth system model simulations show different feedback strengths of the terrestrial carbon cycle under glacial and interglacial conditions, Earth Syst. Dynam., 9, 413–425, https://doi.org/10.5194/esd-9-413-2018, 2018.

Åkesson, H., Morlighem, M., O'Regan, M., and Jakobsson, M.: Future Projections of Petermann Glacier Under Ocean Warming Depend Strongly on Friction Law, JGR Earth Surface, 126, https://doi.org/10.1029/2020JF005921, 2021.

Alvarez-Solas, J., Banderas, R., Robinson, A., and Montoya, M.: Ocean-driven millennial-scale variability of the Eurasian ice sheet during the last glacial period simulated with a hybrid ice-sheet–shelf model, Clim. Past, 15, 957–979, https://doi.org/10.5194/cp-15-957-2019, 2019.

Amante, C.: ETOPO1 1 Arc-Minute Global Relief Model: Procedures, Data Sources and Analysis, https://doi.org/10.7289/V5C8276M, 2009.

Andreassen, K. and Winsborrow, M.: Signature of ice streaming in Bjørnøyrenna, Polar North Atlantic, through the Pleistocene and implications for ice-stream dynamics, Ann. Glaciol., 50, 17–26, https://doi.org/10.3189/172756409789624238, 2009.

Annan, J. D., Hargreaves, J. C., and Mauritsen, T.: A new global surface temperature reconstruction for the Last Glacial Maximum, Clim. Past, 18, 1883–1896, https://doi.org/10.5194/cp-18-1883-2022, 2022.

Anon:, n.d.

Banwell, A. F., MacAyeal, D. R., and Sergienko, O. V.: Breakup of the Larsen B Ice Shelf triggered by chain reaction drainage of supraglacial lakes: LARSEN B CHAIN REACTION LAKE DRAINAGE, Geophys. Res. Lett., 40, 5872–5876, https://doi.org/10.1002/2013GL057694, 2013.

Batchelor, C. L., Margold, M., Krapp, M., Murton, D. K., Dalton, A. S., Gibbard, P. L., Stokes, C. R., Murton, J. B., and Manica, A.: The configuration of Northern Hemisphere ice sheets through the Quaternary, Nat Commun, 10, 3713, https://doi.org/10.1038/s41467-019-11601-2, 2019.

Beckmann, A. and Goosse, H.: A parameterization of ice shelf–ocean interaction for climate models, Ocean Modelling, 5, 157–170, https://doi.org/10.1016/S1463-5003(02)00019-7, 2003.

Beghin, P., Charbit, S., Dumas, C., Kageyama, M., Roche, D. M., and Ritz, C.: Interdependence of the growth of the Northern Hemisphere ice sheets during the last glaciation: the role of atmospheric circulation, Clim. Past, 10, 345–358, https://doi.org/10.5194/cp-10-345-2014, 2014.

Briggs, R. D., Pollard, D., and Tarasov, L.: A data-constrained large ensemble analysis of Antarctic evolution since the Eemian, Quaternary Science Reviews, 103, 91–115, https://doi.org/10.1016/j.quascirev.2014.09.003, 2014.

Brondex, J., Gagliardini, O., Gillet-Chaulet, F., and Durand, G.: Sensitivity of grounding line dynamics to the choice of the friction law, J. Glaciol., 63, 854–866, https://doi.org/10.1017/jog.2017.51, 2017.

Carlson, A. E. and Clark, P. U.: Ice sheet sources of sea level rise and freshwater discharge during the last deglaciation, Rev. Geophys., 50, RG4007, https://doi.org/10.1029/2011RG000371, 2012.

Colleoni, F., Masina, S., Cherchi, A., Navarra, A., Ritz, C., Peyaud, V., and Otto-Bliesner, B.: Modeling Northern Hemisphere ice-sheet distribution during MIS 5 and MIS 7 glacial inceptions, Clim. Past, 10, 269–291, https://doi.org/10.5194/cp-10-269-2014, 2014.

De Rydt, J., Gudmundsson, G. H., Rott, H., and Bamber, J. L.: Modeling the instantaneous response of glaciers after the collapse of the Larsen B Ice Shelf: LARSEN B INSTANTANEOUS SPEEDUP, Geophys. Res. Lett., 42, 5355–5363, https://doi.org/10.1002/2015GL064355, 2015.

Dowdeswell, J. A., Canals, M., Jakobsson, M., Todd, B. J., Dowdeswell, E. K., and Hogan, K. A.: The variety and distribution of submarine glacial landforms and implications for ice-sheet reconstruction, Memoirs, 46, 519–552, https://doi.org/10.1144/M46.183, 2016.

Dowdeswell, J. A., Montelli, A., Akhmanov, G., Solovyeva, M., Terekhina, Y., Mironyuk, S., and Tokarev, M.: Late Weichselian ice-sheet flow directions in the Russian northern Barents Sea from high-resolution imagery of submarine glacial landforms, Geology, 49, 1484–1488, https://doi.org/10.1130/G49252.1, 2021.

Dufresne, J.-L., Foujols, M.-A., Denvil, S., Caubel, A., Marti, O., Aumont, O., Balkanski, Y., Bekki, S., Bellenger, H., Benshila, R., Bony, S., Bopp, L., Braconnot, P., Brockmann, P., Cadule, P., Cheruy, F., Codron, F., Cozic, A., Cugnet, D., de Noblet, N., Duvel, J.-P., Ethé, C., Fairhead, L., Fichefet, T., Flavoni, S., Friedlingstein, P., Grandpeix, J.-Y., Guez, L., Guilyardi, E., Hauglustaine, D., Hourdin, F., Idelkadi, A., Ghattas, J., Joussaume, S., Kageyama, M., Krinner, G., Labetoulle, S., Lahellec, A., Lefebvre, M.-P., Lefevre, F., Levy, C., Li, Z. X., Lloyd, J., Lott, F., Madec, G., Mancip, M., Marchand, M., Masson, S., Meurdesoif, Y., Mignot, J., Musat, I., Parouty, S., Polcher, J., Rio, C., Schulz, M., Swingedouw, D., Szopa, S., Talandier, C., Terray, P., Viovy, N., and Vuichard, N.: Climate change projections using the IPSL-CM5 Earth System Model: from CMIP3 to CMIP5, Clim Dyn, 40, 2123–2165, https://doi.org/10.1007/s00382-012-1636-1, 2013.

Durand, G., Gagliardini, O., de Fleurian, B., Zwinger, T., and Le Meur, E.: Marine ice sheet dynamics: Hysteresis and neutral equilibrium, J. Geophys. Res., 114, F03009, https://doi.org/10.1029/2008JF001170, 2009.

Eyring, V., Bony, S., Meehl, G. A., Senior, C. A., Stevens, B., Stouffer, R. J., and Taylor, K. E.: Overview of the Coupled Model Intercomparison Project Phase 6 (CMIP6) experimental design and organization, Geosci. Model Dev., 9, 1937–1958, https://doi.org/10.5194/gmd-9-1937-2016, 2016.

Frieler, K., Clark, P. U., He, F., Buizert, C., Reese, R., Ligtenberg, S. R. M., van den Broeke, M. R., Winkelmann, R., and Levermann, A.: Consistent evidence of increasing Antarctic accumulation with warming, Nature Clim Change, 5, 348–352, https://doi.org/10.1038/nclimate2574, 2015.

Fürst, J. J., Durand, G., Gillet-Chaulet, F., Tavard, L., Rankl, M., Braun, M., and Gagliardini, O.: The safety band of Antarctic ice shelves, Nature Clim Change, 6, 479–482, https://doi.org/10.1038/nclimate2912, 2016.

Gandy, N., Gregoire, L. J., Ely, J. C., Clark, C. D., Hodgson, D. M., Lee, V., Bradwell, T., and Ivanovic, R. F.: Marine ice sheet instability and ice shelf buttressing of the Minch Ice Stream, northwest Scotland, The Cryosphere, 12, 3635–3651, https://doi.org/10.5194/tc-12-3635-2018, 2018.

Gandy, N., Gregoire, L. J., Ely, J. C., Cornford, S. L., Clark, C. D., and Hodgson, D. M.: Collapse of the Last Eurasian Ice Sheet in the North Sea Modulated by Combined Processes of Ice Flow, Surface Melt, and Marine Ice Sheet Instabilities, J. Geophys. Res. Earth Surf., 126, https://doi.org/10.1029/2020JF005755, 2021.

Goelzer, H., Nowicki, S., Payne, A., Larour, E., Seroussi, H., Lipscomb, W. H., Gregory, J., Abe-Ouchi, A., Shepherd, A., Simon, E., Agosta, C., Alexander, P., Aschwanden, A., Barthel, A., Calov, R., Chambers, C., Choi, Y., Cuzzone, J., Dumas, C., Edwards, T., Felikson, D., Fettweis, X., Golledge, N. R., Greve, R., Humbert, A., Huybrechts, P., Le clec'h, S., Lee, V., Leguy, G., Little, C., Lowry, D. P., Morlighem, M., Nias, I., Quiquet, A., Rückamp, M., Schlegel, N.-J., Slater, D. A., Smith, R. S., Straneo, F., Tarasov, L., van de Wal, R., and van den Broeke, M.: The future sea-level contribution of the Greenland ice sheet: a multi-model ensemble study of ISMIP6, The Cryosphere, 14, 3071–3096, https://doi.org/10.5194/tc-14-3071-2020, 2020.

Gowan, E. J., Zhang, X., Khosravi, S., Rovere, A., Stocchi, P., Hughes, A. L. C., Gyllencreutz, R., Mangerud, J., Svendsen, J.-I., and Lohmann, G.: A new global ice sheet reconstruction for the past 80 000 years, Nat Commun, 12, 1199, https://doi.org/10.1038/s41467-021-21469-w, 2021.

Gudlaugsson, E., Humbert, A., Andreassen, K., Clason, C. C., Kleiner, T., and Beyer, S.: Eurasian ice-sheet dynamics and sensitivity to subglacial hydrology, J. Glaciol., 63, 556–564, https://doi.org/10.1017/jog.2017.21, 2017.

Gudmundsson, G. H.: Ice-shelf buttressing and the stability of marine ice sheets, The Cryosphere, 7, 647–655, https://doi.org/10.5194/tc-7-647-2013, 2013.

Hajima, T., Watanabe, M., Yamamoto, A., Tatebe, H., Noguchi, M. A., Abe, M., Ohgaito, R., Ito, A., Yamazaki, D., Okajima, H., Ito, A., Takata, K., Ogochi, K., Watanabe, S., and Kawamiya, M.: Development of the MIROC-ES2L Earth system model and the evaluation of biogeochemical processes and feedbacks, Geosci. Model Dev., 13, 2197–2244, https://doi.org/10.5194/gmd-13-2197-2020, 2020.

Holland, P. R., Jenkins, A., and Holland, D. M.: The Response of Ice Shelf Basal Melting to Variations in Ocean Temperature, Journal of Climate, 21, 2558–2572, https://doi.org/10.1175/2007JCLI1909.1, 2008.

Hughes, A. L. C., Gyllencreutz, R., Lohne, Ø. S., Mangerud, J., and Svendsen, J. I.: The last Eurasian ice sheets – a chronological database and time-slice reconstruction, DATED-1, Boreas, 45, 1–45, https://doi.org/10.1111/bor.12142, 2016.

Hutter, K.: The Response of a Glacier or an Ice Sheet to Seasonal and Climatic Changes, in: Theoretical Glaciology, Springer Netherlands, Dordrecht, 333–423, https://doi.org/10.1007/978-94-015-1167-4_6, 1983.

Joughin, I., Smith, B. E., and Schoof, C. G.: Regularized Coulomb Friction Laws for Ice Sheet Sliding: Application to Pine Island Glacier, Antarctica, Geophysical Research Letters, 46, 4764–4771, https://doi.org/10.1029/2019GL082526, 2019.

Kageyama, M., Harrison, S. P., Kapsch, M.-L., Lofverstrom, M., Lora, J. M., Mikolajewicz, U., Sherriff-Tadano, S., Vadsaria, T., Abe-Ouchi, A., Bouttes, N., Chandan, D., Gregoire, L. J., Ivanovic, R. F., Izumi, K., LeGrande, A. N., Lhardy, F., Lohmann, G., Morozova, P. A., Ohgaito, R., Paul, A., Peltier, W. R., Poulsen, C. J., Quiquet, A., Roche, D. M., Shi, X., Tierney, J. E., Valdes, P. J., Volodin, E., and Zhu, J.: The PMIP4 Last Glacial Maximum experiments: preliminary results and comparison with the PMIP3 simulations, Clim. Past, 17, 1065–1089, https://doi.org/10.5194/cp-17-1065-2021, 2021.

Kittel, C., Amory, C., Agosta, C., Jourdain, N. C., Hofer, S., Delhasse, A., Doutreloup, S., Huot, P.-V., Lang, C., Fichefet, T., and Fettweis, X.: Diverging future surface mass balance between the Antarctic ice shelves and grounded ice sheet, The Cryosphere, 15, 1215–1236, https://doi.org/10.5194/tc-15-1215-2021, 2021.

Konrad, H., Shepherd, A., Gilbert, L., Hogg, A. E., McMillan, M., Muir, A., and Slater, T.: Net retreat of Antarctic glacier grounding lines, Nature Geosci, 11, 258–262, https://doi.org/10.1038/s41561-018-0082-z, 2018.

Ladant, J.-B., Donnadieu, Y., Lefebvre, V., and Dumas, C.: The respective role of atmospheric carbon dioxide and orbital parameters on ice sheet evolution at the Eocene-Oligocene transition: Ice sheet evolution at the EOT, Paleoceanography, 29, 810–823, https://doi.org/10.1002/2013PA002593, 2014.

Lai, C.-Y., Kingslake, J., Wearing, M. G., Chen, P.-H. C., Gentine, P., Li, H., Spergel, J. J., and van Wessem, J. M.: Vulnerability of Antarctica’s ice shelves to meltwater-driven fracture, Nature, 584, 574–578, https://doi.org/10.1038/s41586-020-2627-8, 2020.

Lambeck, K.: Late Devensian and Holocene shorelines of the British Isles and North Sea from models of glacio-hydro-isostatic rebound, JGS, 152, 437–448, https://doi.org/10.1144/gsjgs.152.3.0437, 1995.

Lambeck, K.: Glaciation and sea-level change for Ireland and the Irish Sea since Late Devensian/Midlandian time, JGS, 153, 853–872, https://doi.org/10.1144/gsjgs.153.6.0853, 1996.

Lambeck, K., Purcell, A., Zhao, J., and Svensson, N.-O.: The Scandinavian Ice Sheet: from MIS 4 to the end of the Last Glacial Maximum, Boreas, 39, 410–435, https://doi.org/10.1111/j.1502-3885.2010.00140.x, 2010.

Lambeck, K., Rouby, H., Purcell, A., Sun, Y., and Sambridge, M.: Sea level and global ice volumes from the Last Glacial Maximum to the Holocene, Proc. Natl. Acad. Sci. U.S.A., 111, 15296–15303, https://doi.org/10.1073/pnas.1411762111, 2014.

Le clec’h, S., Quiquet, A., Charbit, S., Dumas, C., Kageyama, M., and Ritz, C.: A rapidly converging initialisation method to simulate the present-day Greenland ice sheet using the GRISLI ice sheet model (version 1.3), Geosci. Model Dev., 12, 2481–2499, https://doi.org/10.5194/gmd-12-2481-2019, 2019.

Le Meur, E. and Huybrechts, P.: A comparison of different ways of dealing with isostasy: examples from modelling the Antarctic ice sheet during the last glacial cycle, Ann. Glaciol., 23, 309–317, https://doi.org/10.3189/S0260305500013586, 1996.

Liu, Z., Otto-Bliesner, B. L., He, F., Brady, E. C., Tomas, R., Clark, P. U., Carlson, A. E., Lynch-Stieglitz, J., Curry, W., Brook, E., Erickson, D., Jacob, R., Kutzbach, J., and Cheng, J.: Transient Simulation of Last Deglaciation with a New Mechanism for Bølling-Allerød Warming, Science, 325, 310–314, https://doi.org/10.1126/science.1171041, 2009.

MacAyeal, D. R.: Large-scale ice flow over a viscous basal sediment: Theory and application to ice stream B, Antarctica, J. Geophys. Res., 94, 4071–4087, https://doi.org/10.1029/JB094iB04p04071, 1989.

MARGO Project Members: Constraints on the magnitude and patterns of ocean cooling at the Last Glacial Maximum, Nature Geosci, 2, 127–132, https://doi.org/10.1038/ngeo411, 2009a.

MARGO Project Members: Constraints on the magnitude and patterns of ocean cooling at the Last Glacial Maximum, Nature Geosci, 2, 127–132, https://doi.org/10.1038/ngeo411, 2009b.

Marsh, O. J., Fricker, H. A., Siegfried, M. R., Christianson, K., Nicholls, K. W., Corr, H. F. J., and Catania, G.: High basal melting forming a channel at the grounding line of Ross Ice Shelf, Antarctica, Geophysical Research Letters, 43, 250–255, https://doi.org/10.1002/2015GL066612, 2016.

Marshall, S. J., Sharp, M. J., Burgess, D. O., and Anslow, F. S.: Near-surface-temperature lapse rates on the Prince of Wales Icefield, Ellesmere Island, Canada: implications for regional downscaling of temperature, Int. J. Climatol., 27, 385–398, https://doi.org/10.1002/joc.1396, 2007.

Mauritsen, T., Bader, J., Becker, T., Behrens, J., Bittner, M., Brokopf, R., Brovkin, V., Claussen, M., Crueger, T., Esch, M., Fast, I., Fiedler, S., Fläschner, D., Gayler, V., Giorgetta, M., Goll, D. S., Haak, H., Hagemann, S., Hedemann, C., Hohenegger, C., Ilyina, T., Jahns, T., Jimenéz-de-la-Cuesta, D., Jungclaus, J., Kleinen, T., Kloster, S., Kracher, D., Kinne, S., Kleberg, D., Lasslop, G., Kornblueh, L., Marotzke, J., Matei, D., Meraner, K., Mikolajewicz, U., Modali, K., Möbis, B., Müller, W. A., Nabel, J. E. M. S., Nam, C. C. W., Notz, D., Nyawira, S., Paulsen, H., Peters, K., Pincus, R., Pohlmann, H., Pongratz, J., Popp, M., Raddatz, T. J., Rast, S., Redler, R., Reick, C. H., Rohrschneider, T., Schemann, V., Schmidt, H., Schnur, R., Schulzweida, U., Six, K. D., Stein, L., Stemmler, I., Stevens, B., Storch, J., Tian, F., Voigt, A., Vrese, P., Wieners, K., Wilkenskjeld, S., Winkler, A., and Roeckner, E.: Developments in the MPI-M Earth System Model version 1.2 (MPI-ESM1.2) and Its Response to Increasing CO 2, J. Adv. Model. Earth Syst., 11, 998–1038, https://doi.org/10.1029/2018MS001400, 2019.

McManus, J. F., Oppo, D. W., and Cullen, J. L.: A 0.5-Million-Year Record of Millennial-Scale Climate Variability in the North Atlantic, Science, 283, 971–975, https://doi.org/10.1126/science.283.5404.971, 1999.

Mercer, J. H.: Antarctic Ice and Interglacial High Sea Levels, Science, 168, 1605–1606, https://doi.org/10.1126/science.168.3939.1605.b, 1970.

Mouginot, J., Rignot, E., and Scheuchl, B.: Continent-Wide, Interferometric SAR Phase, Mapping of Antarctic Ice Velocity, Geophysical Research Letters, 46, 9710–9718, https://doi.org/10.1029/2019GL083826, 2019.

North Greenland Ice Core Project members: High-resolution record of Northern Hemisphere climate extending into the last interglacial period, Nature, 431, 147–151, https://doi.org/10.1038/nature02805, 2004.

Nowicki, S., Goelzer, H., Seroussi, H., Payne, A. J., Lipscomb, W. H., Abe-Ouchi, A., Agosta, C., Alexander, P., Asay-Davis, X. S., Barthel, A., Bracegirdle, T. J., Cullather, R., Felikson, D., Fettweis, X., Gregory, J. M., Hattermann, T., Jourdain, N. C., Kuipers Munneke, P., Larour, E., Little, C. M., Morlighem, M., Nias, I., Shepherd, A., Simon, E., Slater, D., Smith, R. S., Straneo, F., Trusel, L. D., van den Broeke, M. R., and van de Wal, R.: Experimental protocol for sea level projections from ISMIP6 stand-alone ice sheet models, The Cryosphere, 14, 2331–2368, https://doi.org/10.5194/tc-14-2331-2020, 2020.

Oppo, D. W., McManus, J. F., and Cullen, J. L.: Evolution and demise of the Last Interglacial warmth in the subpolar North Atlantic, Quaternary Science Reviews, 25, 3268–3277, https://doi.org/10.1016/j.quascirev.2006.07.006, 2006.

Patton, H., Hubbard, A., Andreassen, K., Auriac, A., Whitehouse, P. L., Stroeven, A. P., Shackleton, C., Winsborrow, M., Heyman, J., and Hall, A. M.: Deglaciation of the Eurasian ice sheet complex, Quaternary Science Reviews, 169, 148–172, https://doi.org/10.1016/j.quascirev.2017.05.019, 2017.

Pattyn, F.: Sea-level response to melting of Antarctic ice shelves on multi-centennial timescales with the fast Elementary Thermomechanical Ice Sheet model (f.ETISh v1.0), The Cryosphere, 11, 1851–1878, https://doi.org/10.5194/tc-11-1851-2017, 2017.

Pattyn, F.: The paradigm shift in Antarctic ice sheet modelling, Nat Commun, 9, 2728, https://doi.org/10.1038/s41467-018-05003-z, 2018.

Peltier, W. R.: On eustatic sea level history: Last Glacial Maximum to Holocene, Quaternary Science Reviews, 21, 377–396, https://doi.org/10.1016/S0277-3791(01)00084-1, 2002.

Peltier, W. R., Argus, D. F., and Drummond, R.: Space geodesy constrains ice age terminal deglaciation: The global ICE-6G_C (VM5a) model: Global Glacial Isostatic Adjustment, J. Geophys. Res. Solid Earth, 120, 450–487, https://doi.org/10.1002/2014JB011176, 2015.

Petrini, M., Colleoni, F., Kirchner, N., Hughes, A. L. C., Camerlenghi, A., Rebesco, M., Lucchi, R. G., Forte, E., Colucci, R. R., and Noormets, R.: Interplay of grounding-line dynamics and sub-shelf melting during retreat of the Bjørnøyrenna Ice Stream, Sci Rep, 8, 7196, https://doi.org/10.1038/s41598-018-25664-6, 2018.

Petrini, M., Colleoni, F., Kirchner, N., Hughes, A. L. C., Camerlenghi, A., Rebesco, M., Lucchi, R. G., Forte, E., Colucci, R. R., Noormets, R., and Mangerud, J.: Simulated last deglaciation of the Barents Sea Ice Sheet primarily driven by oceanic conditions, Quaternary Science Reviews, 238, 106314, https://doi.org/10.1016/j.quascirev.2020.106314, 2020.

Peyaud, V., Ritz, C., and Krinner, G.: Modelling the Early Weichselian Eurasian Ice Sheets: role of ice shelves and influence of ice-dammed lakes, Clim. Past, 3, 375–386, https://doi.org/10.5194/cp-3-375-2007, 2007.

Pollard, D. and DeConto, R. M.: Modelling West Antarctic ice sheet growth and collapse through the past five million years, Nature, 458, 329–332, https://doi.org/10.1038/nature07809, 2009.

Pollard, D. and DeConto, R. M.: Description of a hybrid ice sheet-shelf model, and application to Antarctica, Geosci. Model Dev., 5, 1273–1295, https://doi.org/10.5194/gmd-5-1273-2012, 2012.

Polyak, L., Forman, S. L., Herlihy, F. A., Ivanov, G., and Krinitsky, P.: Late Weichselian deglacial history of the Svyataya (Saint) Anna Trough, northern Kara Sea, Arctic Russia, Marine Geology, 143, 169–188, https://doi.org/10.1016/S0025-3227(97)00096-0, 1997.

Pritchard, H. D., Arthern, R. J., Vaughan, D. G., and Edwards, L. A.: Extensive dynamic thinning on the margins of the Greenland and Antarctic ice sheets, Nature, 461, 971–975, https://doi.org/10.1038/nature08471, 2009.

Pritchard, H. D., Ligtenberg, S. R. M., Fricker, H. A., Vaughan, D. G., van den Broeke, M. R., and Padman, L.: Antarctic ice-sheet loss driven by basal melting of ice shelves, Nature, 484, 502–505, https://doi.org/10.1038/nature10968, 2012.

Quiquet, A. and Dumas, C.: The GRISLI-LSCE contribution to the Ice Sheet Model Intercomparison Project for phase 6 of the Coupled Model Intercomparison Project (ISMIP6) – Part 1: Projections of the Greenland ice sheet evolution by the end of the 21st century, The Cryosphere, 15, 1015–1030, https://doi.org/10.5194/tc-15-1015-2021, 2021a.

Quiquet, A. and Dumas, C.: The GRISLI-LSCE contribution to the Ice Sheet Model Intercomparison Project for phase 6 of the Coupled Model Intercomparison Project (ISMIP6) – Part 2: Projections of the Antarctic ice sheet evolution by the end of the 21st century, The Cryosphere, 15, 1031–1052, https://doi.org/10.5194/tc-15-1031-2021, 2021b.

Quiquet, A., Ritz, C., Punge, H. J., and Salas y Mélia, D.: Greenland ice sheet contribution to sea level rise during the last interglacial period: a modelling study driven and constrained by ice core data, Clim. Past, 9, 353–366, https://doi.org/10.5194/cp-9-353-2013, 2013.

Quiquet, A., Dumas, C., Ritz, C., Peyaud, V., and Roche, D. M.: The GRISLI ice sheet model (version 2.0): calibration and validation for multi-millennial changes of the Antarctic ice sheet, Geosci. Model Dev., 11, 5003–5025, https://doi.org/10.5194/gmd-11-5003-2018, 2018.

Quiquet, A., Roche, D. M., Dumas, C., Bouttes, N., and Lhardy, F.: Climate and ice sheet evolutions from the last glacial maximum to the pre-industrial period with an ice-sheet–climate coupled model, Clim. Past, 17, 2179–2199, https://doi.org/10.5194/cp-17-2179-2021, 2021.

Rasmussen, T. L. and Thomsen, E.: Climate and ocean forcing of ice-sheet dynamics along the Svalbard-Barents Sea ice sheet during the deglaciation ~20,000–10,000 years BP, Quaternary Science Advances, 3, 100019, https://doi.org/10.1016/j.qsa.2020.100019, 2021.

Rignot, E.: Accelerated ice discharge from the Antarctic Peninsula following the collapse of Larsen B ice shelf, Geophys. Res. Lett., 31, L18401, https://doi.org/10.1029/2004GL020697, 2004.

Rignot, E., Mouginot, J., Scheuchl, B., van den Broeke, M., van Wessem, M. J., and Morlighem, M.: Four decades of Antarctic Ice Sheet mass balance from 1979–2017, Proc. Natl. Acad. Sci. U.S.A., 116, 1095–1103, https://doi.org/10.1073/pnas.1812883116, 2019.

Ritz, C., Rommelaere, V., and Dumas, C.: Modeling the evolution of Antarctic ice sheet over the last 420,000 years: Implications for altitude changes in the Vostok region, J. Geophys. Res., 106, 31943–31964, https://doi.org/10.1029/2001JD900232, 2001.

Schoof, C.: Marine ice sheet stability, J. Fluid Mech., 698, 62–72, https://doi.org/10.1017/jfm.2012.43, 2012.

Sejrup, H. P., Haflidason, H., Aarseth, I., King, E., Forsberg, C. F., Long, D., and Rokoengen, K.: Late Weichselian glaciation history of the northern North Sea, Boreas, 23, 1–13, https://doi.org/10.1111/j.1502-3885.1994.tb00581.x, 2008.

Sejrup, H. P., Hjelstuen, B. O., Patton, H., Esteves, M., Winsborrow, M., Rasmussen, T. L., Andreassen, K., and Hubbard, A.: The role of ocean and atmospheric dynamics in the marine-based collapse of the last Eurasian Ice Sheet, Commun Earth Environ, 3, 119, https://doi.org/10.1038/s43247-022-00447-0, 2022.

Sepulchre, P., Caubel, A., Ladant, J.-B., Bopp, L., Boucher, O., Braconnot, P., Brockmann, P., Cozic, A., Donnadieu, Y., Dufresne, J.-L., Estella-Perez, V., Ethé, C., Fluteau, F., Foujols, M.-A., Gastineau, G., Ghattas, J., Hauglustaine, D., Hourdin, F., Kageyama, M., Khodri, M., Marti, O., Meurdesoif, Y., Mignot, J., Sarr, A.-C., Servonnat, J., Swingedouw, D., Szopa, S., and Tardif, D.: IPSL-CM5A2 – an Earth system model designed for multi-millennial climate simulations, Geosci. Model Dev., 13, 3011–3053, https://doi.org/10.5194/gmd-13-3011-2020, 2020.

Seroussi, H., Nowicki, S., Payne, A. J., Goelzer, H., Lipscomb, W. H., Abe-Ouchi, A., Agosta, C., Albrecht, T., Asay-Davis, X., Barthel, A., Calov, R., Cullather, R., Dumas, C., Galton-Fenzi, B. K., Gladstone, R., Golledge, N. R., Gregory, J. M., Greve, R., Hattermann, T., Hoffman, M. J., Humbert, A., Huybrechts, P., Jourdain, N. C., Kleiner, T., Larour, E., Leguy, G. R., Lowry, D. P., Little, C. M., Morlighem, M., Pattyn, F., Pelle, T., Price, S. F., Quiquet, A., Reese, R., Schlegel, N.-J., Shepherd, A., Simon, E., Smith, R. S., Straneo, F., Sun, S., Trusel, L. D., Van Breedam, J., van de Wal, R. S. W., Winkelmann, R., Zhao, C., Zhang, T., and Zwinger, T.: ISMIP6 Antarctica: a multi-model ensemble of the Antarctic ice sheet evolution over the 21st century, The Cryosphere, 14, 3033–3070, https://doi.org/10.5194/tc-14-3033-2020, 2020.

Shapiro, N.: Inferring surface heat flux distributions guided by a global seismic model: particular application to Antarctica, Earth and Planetary Science Letters, 223, 213–224, https://doi.org/10.1016/j.epsl.2004.04.011, 2004.

Solgaard, A., Kusk, A., Merryman Boncori, J. P., Dall, J., Mankoff, K. D., Ahlstrøm, A. P., Andersen, S. B., Citterio, M., Karlsson, N. B., Kjeldsen, K. K., Korsgaard, N. J., Larsen, S. H., and Fausto, R. S.: Greenland ice velocity maps from the PROMICE project, Earth Syst. Sci. Data, 13, 3491–3512, https://doi.org/10.5194/essd-13-3491-2021, 2021.

Stokes, C.: Palaeo-ice streams, Quaternary Science Reviews, 20, 1437–1457, https://doi.org/10.1016/S0277-3791(01)00003-8, 2001.

Sueyoshi, T., Ohgaito, R., Yamamoto, A., Chikamoto, M. O., Hajima, T., Okajima, H., Yoshimori, M., Abe, M., O'ishi, R., Saito, F., Watanabe, S., Kawamiya, M., and Abe-Ouchi, A.: Set-up of the PMIP3 paleoclimate experiments conducted using an Earth system model, MIROC-ESM, Geosci. Model Dev., 6, 819–836, https://doi.org/10.5194/gmd-6-819-2013, 2013.

Svendsen, J. I., Alexanderson, H., Astakhov, V. I., Demidov, I., Dowdeswell, J. A., Funder, S., Gataullin, V., Henriksen, M., Hjort, C., Houmark-Nielsen, M., Hubberten, H. W., Ingólfsson, Ó., Jakobsson, M., Kjær, K. H., Larsen, E., Lokrantz, H., Lunkka, J. P., Lyså, A., Mangerud, J., Matiouchkov, A., Murray, A., Möller, P., Niessen, F., Nikolskaya, O., Polyak, L., Saarnisto, M., Siegert, C., Siegert, M. J., Spielhagen, R. F., and Stein, R.: Late Quaternary ice sheet history of northern Eurasia, Quaternary Science Reviews, 23, 1229–1271, https://doi.org/10.1016/j.quascirev.2003.12.008, 2004.

Svendsen, J. I., Briner, J. P., Mangerud, J., and Young, N. E.: Early break-up of the Norwegian Channel Ice Stream during the Last Glacial Maximum, Quaternary Science Reviews, 107, 231–242, https://doi.org/10.1016/j.quascirev.2014.11.001, 2015.

Szuman, I., Kalita, J. Z., Ewertowski, M. W., Clark, C. D., and Livingstone, S. J.: Dynamics of the last Scandinavian Ice Sheet's southernmost sector revealed by the pattern of ice streams, Boreas, 50, 764–780, https://doi.org/10.1111/bor.12512, 2021.

Tarasov, L. and Richard Peltier, W.: Greenland glacial history and local geodynamic consequences, Geophysical Journal International, 150, 198–229, https://doi.org/10.1046/j.1365-246X.2002.01702.x, 2002.

Tarasov, L., Dyke, A. S., Neal, R. M., and Peltier, W. R.: A data-calibrated distribution of deglacial chronologies for the North American ice complex from glaciological modeling, Earth and Planetary Science Letters, 315–316, 30–40, https://doi.org/10.1016/j.epsl.2011.09.010, 2012.

Tierney, J. E., Zhu, J., King, J., Malevich, S. B., Hakim, G. J., and Poulsen, C. J.: Glacial cooling and climate sensitivity revisited, Nature, 584, 569–573, https://doi.org/10.1038/s41586-020-2617-x, 2020.

Tsai, V. C. and Gudmundsson, G. H.: An improved model for tidally modulated grounding-line migration, J. Glaciol., 61, 216–222, https://doi.org/10.3189/2015JoG14J152, 2015.

Ullman, D. J., LeGrande, A. N., Carlson, A. E., Anslow, F. S., and Licciardi, J. M.: Assessing the impact of Laurentide Ice Sheet topography on glacial climate, Clim. Past, 10, 487–507, https://doi.org/10.5194/cp-10-487-2014, 2014.

Voldoire, A., Sanchez-Gomez, E., Salas y Mélia, D., Decharme, B., Cassou, C., Sénési, S., Valcke, S., Beau, I., Alias, A., Chevallier, M., Déqué, M., Deshayes, J., Douville, H., Fernandez, E., Madec, G., Maisonnave, E., Moine, M.-P., Planton, S., Saint-Martin, D., Szopa, S., Tyteca, S., Alkama, R., Belamari, S., Braun, A., Coquart, L., and Chauvin, F.: The CNRM-CM5.1 global climate model: description and basic evaluation, Clim Dyn, 40, 2091–2121, https://doi.org/10.1007/s00382-011-1259-y, 2013.

Weertman, J.: On the Sliding of Glaciers, J. Glaciol., 3, 33–38, https://doi.org/10.3189/S0022143000024709, 1957.

Winkelmann, R., Martin, M. A., Haseloff, M., Albrecht, T., Bueler, E., Khroulev, C., and Levermann, A.: The Potsdam Parallel Ice Sheet Model (PISM-PIK) – Part 1: Model description, The Cryosphere, 5, 715–726, https://doi.org/10.5194/tc-5-715-2011, 2011.

Yukimoto, S., Adachi, Y., Hosaka, M., Sakami, T., Yoshimura, H., Hirabara, M., Tanaka, T. Y., Shindo, E., Tsujino, H., Deushi, M., Mizuta, R., Yabu, S., Obata, A., Nakano, H., Koshiro, T., Ose, T., and Kitoh, A.: A New Global Climate Model of the Meteorological Research Institute: MRI-CGCM3 —Model Description and Basic Performance—, Journal of the Meteorological Society of Japan, 90A, 23–64, https://doi.org/10.2151/jmsj.2012-A02, 2012.

Zheng, W. and Yu, Y.: Paleoclimate simulations of the mid-Holocene and last glacial maximum by FGOALS, Adv. Atmos. Sci., 30, 684–698, https://doi.org/10.1007/s00376-012-2177-6, 2013.

Zwally, H. J., Li, J., Robbins, J. W., Saba, J. L., Yi, D., and Brenner, A. C.: Mass gains of the Antarctic ice sheet exceed losses, J. Glaciol., 61, 1019–1036, https://doi.org/10.3189/2015JoG15J071, 2015.